

# Experimental study of inertial particles clustering and settling in homogeneous turbulence

Alec J. Petersen<sup>1,2,†</sup>, Lucia Baker<sup>1,2</sup> and Filippo Coletti<sup>1,2</sup>

<sup>1</sup>Department of Aerospace Engineering and Mechanics, University of Minnesota,  
Minneapolis, MN 55414, USA

<sup>2</sup>St. Anthony Falls Laboratory, University of Minnesota, Minneapolis, MN 55414, USA

(Received 11 August 2018; revised 1 December 2018; accepted 30 December 2018;  
first published online 14 February 2019)

We study experimentally the spatial distribution, settling and interaction of sub-Kolmogorov inertial particles with homogeneous turbulence. Utilizing a zero-mean-flow air turbulence chamber, we drop size-selected solid particles and study their dynamics with particle imaging and tracking velocimetry at multiple resolutions. The carrier flow is simultaneously measured by particle image velocimetry of suspended tracers, allowing the characterization of the interplay between both the dispersed and continuous phases. The turbulence Reynolds number based on the Taylor microscale ranges from  $Re_\lambda \approx 200\text{--}500$ , while the particle Stokes number based on the Kolmogorov scale varies between  $St_\eta = O(1)$  and  $O(10)$ . Clustering is confirmed to be most intense for  $St_\eta \approx 1$ , but it extends over larger scales for heavier particles. Individual clusters form a hierarchy of self-similar, fractal-like objects, preferentially aligned with gravity and with sizes that can reach the integral scale of the turbulence. Remarkably, the settling velocity of  $St_\eta \approx 1$  particles can be several times larger than the still-air terminal velocity, and the clusters can fall even faster. This is caused by downward fluid fluctuations preferentially sweeping the particles, and we propose that this mechanism is influenced by both large and small scales of the turbulence. The particle–fluid slip velocities show large variance, and both the instantaneous particle Reynolds number and drag coefficient can greatly differ from their nominal values. Finally, for sufficient loadings, the particles generally augment the small-scale fluid velocity fluctuations, which however may account for a limited fraction of the turbulent kinetic energy.

**Key words:** homogeneous turbulence, particle/fluid flows

---

## 1. Introduction

The dynamics of particles carried by turbulent fluid flows is rich with fascinating phenomena. This is true even for the highly simplified case we consider: homogeneous incompressible turbulence laden with a dilute concentration of spherical, non-Brownian particles smaller than the Kolmogorov scale. The behaviour is especially complex

† Email address for correspondence: [pet00105@umn.edu](mailto:pet00105@umn.edu)

when the particles are inertial without being ballistic, i.e. their aerodynamic response time  $\tau_p$  is comparable to some relevant temporal scale of the flow. Several important effects observed in this regime are summarized below, making no claim of being exhaustive. For more details the reader is referred to recent reviews from Poelma & Ooms (2006), Balachandar & Eaton (2010) and Gustavsson & Mehlig (2016).

Inertial particles do not distribute homogeneously in turbulent flows, favouring regions of high strain and low vorticity (Maxey 1987; Squires & Eaton 1991*b*). Such preferential concentration is consistent with early observations of particles accumulating outside the core of large-scale rollers and vortex rings in shear layers and jets (Lázaro & Lasherás 1989; Longmire & Eaton 1992; Ishima, Hishida & Maeda 1993), and has been attributed to the action of vortices centrifuging the particles outside of their core (Eaton & Fessler 1994). While this tendency is noticeable even for weakly inertial particles, it is most intense when the Stokes number based on the Kolmogorov time scale ( $St_\eta = \tau_p/\tau_\eta$ ) is close to unity (Wang & Maxey 1993). Such a result is understood as a consequence of  $\tau_\eta$  being the scale at which the highest vorticity occurs, and indeed particles with  $St_\eta \approx 1$  were reported to form clusters scaling in Kolmogorov units (Kulick, Fessler & Eaton 1994; Aliseda *et al.* 2002). This interpretation also implies that more inertial particles should cluster around eddies of larger turnover times, as was indeed shown by Yoshimoto & Goto (2007) who reported multi-scale preferential concentration from the dissipative to the inertial range. However, clustering of particles with  $St_\eta$  significantly larger than unity displays different features compared to less inertial ones (Bec *et al.* 2007), and mechanisms other than the centrifugal effect have been proposed (Goto & Vassilicos 2008; Bragg & Collins 2014; Ireland, Bragg & Collins 2016*a*).

An important effect of the particle inertia is that, as the particles depart from the fluid streamlines, they may collide. The collision probability is a function of both the local concentration and the relative velocity (Sundaram & Collins 1997; Wang, Wexler & Zhou 2000) the latter being potentially large as particles approach each other from different flow regions (Falkovich, Fouxon & Stepanov 2002; Wilkinson & Mehlig 2005; Bewley, Saw & Bodenschatz 2013). When the particles are liquid droplets, collisions can lead to breakup or coalescence, with important implications for, e.g. atmospheric clouds (Shaw 2003) and spray combustion (Jenny, Roekaerts & Beishuizen 2012). Additionally, in the presence of gravity, the drift of heavy particles crossing fluid trajectories decorrelates their motion from the turbulent fluctuations (Yudine 1959; Csanady 1963), reducing the particle velocity autocorrelation and dispersion coefficient (Reeks 1977; Wells & Stock 1983; Squires & Eaton 1991*a*; Elghobashi & Truesdell 1992).

Beside concentration effects, a major consequence of turbulence in particle-laden flows is to alter the rate of gravitational settling. In their seminal work, Wang & Maxey (1993) confirmed by direct numerical simulations (DNS) the ideas put forward by Maxey (1987) using Gaussian flow simulations, and identified a mechanism by which inertial particles with  $St_\eta = O(1)$  oversample downward regions of the turbulent eddies. This process, referred to as preferential sweeping or fast tracking, can lead to a significant increase in mean fall speed compared to the expected terminal velocity in quiescent or laminar fluids,  $W_0 = \tau_p g$  ( $g$  is the gravitational acceleration). Other mechanisms by which turbulence may modify the settling velocity have been proposed, as reviewed by Nielsen (1993) and Good, Gerashchenko & Warhaft (2012). These include: vortex trapping, by which relatively light particles are trapped in vortical orbits (Tooby, Wick & Isaacs 1977); loitering, due to fast-falling particles spending more time in updrafts than in downdrafts (Nielsen 1993; Kawanisi & Shiozaki 2008);

and nonlinear drag increase, which may reduce the travelling speed of particles with significant Reynolds number based on their diameter and slip velocity (Mei, Adrian & Hanratty 1991; Mei 1994); all of these can lead to a decrease in mean fall speed, as opposed to preferential sweeping. Additionally, local hydrodynamic interactions between particles were shown to increase fall speed of bi-disperse suspensions (Wang, Ayala & Grabowski 2007). While the conditions under which these mechanisms manifest are not well known, enhanced settling due to preferential sweeping appears to be prevalent for sub-Kolmogorov particles with  $St_\eta = O(1)$  (Yang & Lei 1998; Aliseda *et al.* 2002; Yang & Shy 2003; Dejoan & Monchaux 2013; Good *et al.* 2014; Ireland, Bragg & Collins 2016*b*; Rosa *et al.* 2016; Baker *et al.* 2017). Still, there is no consensus on which turbulence scales are most relevant for this process.

Though several works reported settling enhancement by turbulence under similar flow conditions, its extent remains an open question. In numerical simulations, the maximum increase of vertical velocity (which most authors found for  $St_\eta \approx 1$ ) varies between studies, from approximately  $0.1W_0$  to  $0.9W_0$ , or between  $0.04u'$  and  $0.16u'$ ,  $u'$  being the root-mean-square (r.m.s.) fluid velocity fluctuation (Wang & Maxey 1993; Yang & Lei 1998; Dejoan & Monchaux 2013; Bec, Homann & Ray 2014*a*; Good *et al.* 2014; Baker *et al.* 2017). Laboratory observations have shown unsatisfactory quantitative agreement with simulations, and between each other. Aliseda *et al.* (2002) found strong increases in settling velocity of spray droplets in grid turbulence, as high as  $1.6W_0$  or  $0.26u'$  for their most dilute case. Later, Yang & Shy (2003, 2005) reported much weaker settling enhancement for solid particles in zero-mean-flow turbulence facilities. This led Bosse & Kleiser (2006), comparing their simulations to the results of both groups, to speculate on possible sources of errors in the measurements of Aliseda *et al.* (2002). Good *et al.* (2012) also found dramatic increases of spray droplet fall speed with turbulence, but this was amplified by mean-flow effects (Good *et al.* 2014). In a subsequent study, Good *et al.* (2014), using an extensively tested zero-mean-flow apparatus and high-resolution imaging, found levels of settling enhancement comparable with Aliseda *et al.* (2002). But they also showed that point-particle DNS at matching conditions yielding only qualitative agreement with the measurements. In a recent field study Nemes *et al.* (2017) measured the fall speed of compact snowflakes by high-speed imaging. They estimated the Stokes number of the observed snowflakes as  $St_\eta \approx 0.1\text{--}0.4$ , and concluded that the settling velocity in atmospheric turbulence was several times larger than the expected still-air fall speed.

An aspect of particle-laden turbulent flows in which our understanding is particularly incomplete is the backreaction of the dispersed phase on the fluid. There is substantial evidence that particles can alter the turbulent fluctuations, but it is still debated under which conditions these will be excited or inhibited (Balachandar & Eaton 2010). Gore & Crowe (1991) argued that turbulence intensity is augmented/attenuated by particles larger/smaller than one tenth of the integral scale. For fully developed turbulence, this threshold concerns particles significantly larger than the Kolmogorov scale, which will likely modify the turbulence by locally distorting energetic eddies. Hetsroni (1989) proposed a criterion based on the particle Reynolds number  $Re_p = d_p U_{slip}/\nu$  (where  $d_p$  is the particle diameter,  $\nu$  is the kinematic viscosity and  $U_{slip}$  is the slip velocity between both phases), predicting augmented and attenuated turbulence for  $Re_p > 400$  and  $Re_p < 100$ , respectively. These thresholds are also relevant to relatively large particles. Elghobashi (1994) indicated that turbulence modification occurred when the volume fraction  $\phi_v$  is higher than approximately  $10^{-6}$ . In the presence of preferential concentration, however, the local volume fraction

can be much higher than the mean, enhancing collective effects within and around the clusters (Aliseda *et al.* 2002). More recently, Huck *et al.* (2018) showed that by conditioning on the local volume fraction, they could identify three regimes affecting the settling velocity: the sparsest dominated by the background flow, the intermediate concentrations suggesting preferential concentration effects and the densest clusters triggering collective drag. Other parameters have been found to be consequential, including the Stokes number and the particle-to-fluid density ratio  $\rho_p/\rho_f$ , pointing to the multifaceted nature of the problem (Poelma, Westerweel & Ooms 2007; Tanaka & Eaton 2008). The question of turbulence augmentation versus attenuation is complicated by the fact that the particle–fluid energy transfer is scale dependent: several studies found that the presence of inertial particles increases the energy at small scales and decreases it at large scales (Elghobashi & Truesdell 1993; Boivin, Simonin & Squires 1998; Sundaram & Collins 1999; Ferrante & Elghobashi 2003; Poelma *et al.* 2007). Gravitational settling also contributes to the turbulence modification, as the falling particles transfer their potential energy to the fluid (Yang & Shy 2005; Hwang & Eaton 2006b; Frankel *et al.* 2016).

Both simulating this class of flows and measuring their properties are challenging. From the computational standpoint, the representation of the particle phase is not straightforward. Since the seminal work of Eaton and Elghobashi, a widespread approach has been to model particles as material points and track their Lagrangian trajectories through the Eulerian flow field obtained by DNS. This led to groundbreaking insights, both when treating the particles as passively advected by the fluid (one-way coupling, Squires & Eaton 1991b; Elghobashi & Truesdell 1992) and when including their backreaction on the fluid (two-way coupling, Squires & Eaton 1990; Elghobashi & Truesdell 1993). This approach, however, has well-known limitations. The particle equation of motion assuming Stokes drag (even with the correction terms derived by Maxey & Riley (1983)) is only applicable when particles are much smaller than Kolmogorov scale, and finite- $Re_p$  effects are minimal. Indeed, although the one-way-coupled DNS has led to overall agreement with experiments (e.g. for Lagrangian accelerations, Ayyalasomayajula *et al.* (2006), Bec *et al.* (2006)), quantitative discrepancies indicate that the Stokes drag model may miss important dynamics (Saw *et al.* 2014). Moreover, modelling the backreaction of the dispersed phase by point-particle methods present technical issues associated with the application of the point-wise forcing on the fluid computational grid (Balachandar 2009; Eaton 2009; Gualtieri *et al.* 2013). To overcome these shortcomings, advanced methods have recently been proposed (Gualtieri *et al.* 2015; Horwitz & Mani 2016; Ireland & Desjardins 2017) whose merits need to be fully appreciated in future comparisons with well-controlled experiments. Setting up the turbulent flow in two-way coupled simulations is also a critical issue: forcing steady-state homogeneous turbulence in either Fourier or physical space leads to artificial energy transfers hardly discernible from the actual interphase dynamics (Lucci, Frante & Elghobashi 2010). Decaying turbulence leaves the natural coupling unaltered, but quickly drops to low Reynolds numbers and complicates the extraction of statistical quantities.

Laboratory measurements also present significant challenges, especially to extract the fluid flow information. Techniques such as laser Doppler velocimetry (LDV), particle image velocimetry (PIV) and particle tracking velocimetry (PTV) require tracers that need to be discriminated from the inertial particles. This can be achieved in LDV by signal-processing schemes (Rogers & Eaton 1991; Kulick *et al.* 1994), which are relatively complicated and require careful adjustment (Balachandar & Eaton 2010). Moreover, single-point techniques as LDV cannot capture the flow structures

and particle clusters that are essential in the dynamics, and as such they have been superseded by whole-field methods, either by conventional or holographic imaging. Time-resolved three-dimensional PTV (often termed Lagrangian particle tracking) has been successfully used to investigate inertial particle acceleration (Ayyalasomayajula *et al.* 2006; Gerashchenko *et al.* 2008; Volk *et al.* 2008), dispersion (Sabban & van Hout 2011), relative velocity (Bewley *et al.* 2013; Saw *et al.* 2014) and collision rates (Bordás *et al.* 2013). A limitation of this approach is the low particle concentration needed for unambiguous stereo-matching from multiple cameras; this has prevented the volumetric investigation of clustering. For the same reason, experimental studies where both inertial particles and fluid tracers are captured in three dimensions are scarce (Guala *et al.* (2008) being a rare exception). Two-dimensional (2-D) imaging has proven capable of capturing inertial particle distributions and velocities as well as the underlying flow field. Clustering has been probed by 2-D imaging since Fessler, Kulick & Eaton (1994), and multiple approaches have since been utilized to characterize concentration fields, as reviewed by Monchaux, Bourgoin & Cartellier (2012). To obtain two-phase measurements, the fluid tracers and inertial particles can be discriminated based on their image size and intensity (Khalitov & Longmire 2002) and digital/optical filtering (Kiger & Pan 2000; Poelma *et al.* 2007). The motion of the continuous and dispersed phases is then characterized by PIV and PTV, respectively. This approach has allowed the investigation of particle–turbulence interaction in wall-bounded (Paris 2001; Kiger & Pan 2002; Khalitov & Longmire 2003) and homogeneous flows (Yang & Shy 2003, 2005; Hwang & Eaton 2006a; Poelma *et al.* 2007; Tanaka & Eaton 2010; Sahu, Hardalupas & Taylor 2014, 2016). Many of these studies were obtained for relatively large particles, for which significant loadings are obtained with limited number densities. Sub-Kolmogorov particles are harder to discriminate from tracers, and the velocimetry of the surrounding fluid is especially challenging in presence of clusters (Yang & Shy 2005).

We present the results of an extensive measurement campaign in which sub-Kolmogorov solid particles settle in homogeneous air turbulence created in a zero-mean-flow chamber. Planar imaging at various resolutions is used to probe both dispersed and continuous phases over a wide range of scales, providing insight into several of the outstanding questions discussed above. The paper is organized as follows: the experimental apparatus, the measurement approach and the parameter space are described in § 2. The particle spatial distribution and clustering are described in § 3, whereas the effect of turbulence on their fall speed is addressed in § 4. In § 5 the simultaneous two-phase measurements are leveraged to explore the particle–turbulence interaction. A discussion of the results and conclusions drawn from them are given in § 6.

## 2. Methods

### 2.1. Experimental apparatus

The experimental facility consists of a chamber where homogeneous air turbulence is produced by jet arrays, and in which known quantities of size-selected solid particles are dropped. The turbulence chamber has been introduced and qualified in Carter *et al.* (2016) and the unladen flow properties have been investigated in detail in Carter & Coletti (2017, 2018); here we only give a brief description for completeness. The 5 m<sup>3</sup> closed chamber has acrylic lateral walls and ceiling for optical access, and it contains two facing arrays of 256 quasi-synthetic jets controlled by individual solenoid valves. Using the jet firing sequence proposed by Variano & Cowen (2008), we obtain

Grids	$\mu_{on}$ (s)	$u'$ (m s <sup>-1</sup> )	$u'_x/u'_z$	$L$ (mm)	$\eta$ (mm)	$\tau_\eta$ (ms)	$Re_\lambda$
Yes	0.4	0.34	1.41	73	0.34	7.5	200
Yes	10.0	0.51	1.72	100	0.28	4.9	300
No	0.2	0.59	1.41	90	0.27	4.8	300
No	0.4	0.67	1.46	99	0.24	3.8	360
No	3.2	0.73	1.72	140	0.24	3.6	500
No	10.0	0.76	1.67	146	0.24	3.6	500

TABLE 1. Unladen turbulence statistics for the configurations in this study. The r.m.s. velocity  $u'$  and the longitudinal integral scale  $L$  are based on a weighted average between the  $x$  and  $z$  directions. The Kolmogorov length scale  $\eta = (v^3/\varepsilon)^{1/4}$  and time scale  $\tau_\eta = (\nu/\varepsilon)^{1/2}$  are based on estimates of the dissipation rate  $\varepsilon$  from the second-order transverse structure functions. For further details see Carter *et al.* (2016).

approximately homogeneous turbulence with negligible mean flow and no shear over a central region of 0.5 by 0.4 by 0.7 m<sup>3</sup> in direction  $x$ ,  $y$  and  $z$ , respectively (where  $x$  is aligned with the jet axis and  $z$  is vertical). This is substantially larger than the integral scale of the flow, allowing for the natural inter-scale energy transfer without major effects of the boundary conditions. Importantly, this also means that the particles, remembering the flow they experience through the history term in their transport equation (Maxey & Riley 1983), are not affected by turbulence inhomogeneity. The lack of mean flow (especially small in the vertical direction, see Carter *et al.* 2016) is beneficial for the unbiased measurement of the particle settling velocity. The properties of the turbulence can be adjusted by varying the average jet firing time  $\mu_{on}$ , the distance between both jet arrays, and by adding grids in front of the jets. In the present study, we keep the distance at 1.81 m and use a combination of firing times and grids that force turbulence with a Taylor microscale Reynolds number  $Re_\lambda \approx 200\text{--}500$ ; the main properties for the unladen flow are reported in table 1. These may be altered by the presence of particles, although not dramatically in the considered range of particle types and loadings, as we will discuss in § 5. The flow is anisotropic at all scales, with more intense velocity fluctuations in the  $x$  direction (Carter & Coletti 2017). The fine-scale structure and topology display all signature features of homogeneous turbulence (Carter & Coletti 2018).

The chamber ceiling is provided with a circular opening (15.2 cm in diameter) connected to a 3 m vertical chute, through which solid particles are introduced at a steady rate using an AccuRate dry material feeder. The feeding rate is adjusted to produce different volume fractions in the chamber. The particles interact with the turbulence for at least 0.7 m before entering the field of view (FOV). At typical settling rates and depending on the particle types, this corresponds to between tens and hundreds of integral time scales of the turbulence, corroborating our observation that the particles spread throughout the chamber quickly upon entering it. We use several types of particles: soda-lime glass beads of various sizes (Mo-Sci Corp.), lycopodium spores (Flinn Scientific, Inc.) and glass bubbles (The 3M Company), all with a high degree of sphericity as verified by optical microscopy. The properties of the considered particle types are listed in table 2. The aerodynamic response time is iteratively calculated with the Schiller & Naumann correction (Clift, Grace & Weber 2005)):

$$\tau_p = \frac{\rho_p d_p^2}{18\mu(1 + 0.15Re_{p,0}^{0.687})}, \quad (2.1)$$

$d_p$ ( $\mu\text{m}$ )	Material	$\rho_p$ ( $\text{kg cm}^{-3}$ )	$\tau_p$ (ms)	$Re_{p,0}$
$91 \pm 11$	Glass bubbles	100	1.7	0.10
$30 \pm 2$	Lycopodium	1200	3.1	0.06
$32 \pm 7$	Glass	2500	7.4	0.15
$52 \pm 6.1$	Glass	2500	17	0.56
$96 \pm 11$	Glass	2500	47	3.26

TABLE 2. Particle properties. The diameters  $d_p$  are listed in mean  $\pm$  standard deviation.

where  $\mu$  is the air dynamic viscosity,  $\rho_p$  and  $d_p$  are the particle density and mean diameter and  $Re_{p,0} = d_p W_0 / \nu$  is the particle Reynolds number based on the still-air settling velocity.

## 2.2. Measurement techniques

All measurements are performed along the  $x$ - $z$  symmetry plane, using the same hardware as in Carter *et al.* (2016) and Carter & Coletti (2017, 2018). The air flow is seeded with 1–2  $\mu\text{m}$  DEHS (di-ethyl-hexyl-sebacate) droplets, which are small enough to faithfully trace the air motion without altering the particle transport. The imaging system consists of a dual-head Nd:YAG laser (532 nm wavelength, 200 mJ pulse $^{-1}$ ) synchronized with a 4 Mpixel, 12-bit CCD camera. To capture the wide range of spatial scales, we perform measurements using Nikon lenses with focal lengths of 50, 105 and 200 mm, yielding a range of FOVs and resolutions reported in table 3. The laser pulse separation, chosen as a compromise to capture the in-plane motion of both flow tracers and inertial particles, ranges between 110  $\mu\text{s}$  (to image the heavier particles in the smaller FOV and stronger turbulence) and 850  $\mu\text{s}$  (for the lighter particles in the larger FOV in weaker turbulence). For all measurements the typical displacement of both tracers and inertial particles is approximately 5 pixels. For the inertial particles this corresponds to 1 visual particle diameter on average. The sampling frequency is 7.25 Hz, which provides approximately uncorrelated realizations (given the typical large-eddy turnover time between 0.1 and 0.2 s). For most experiments, 2000 image pairs are recorded. For the cases with highest loading, the finite supply of particles in the screw-feeder limits the recordings to 1000–1500 image pairs. Because those cases also have the highest number of particles per image (and do not allow accurate fluid measurements), the statistical convergence of the reported quantities is not significantly altered.

The two-phase flow images are used to perform simultaneous PIV on the tracers and PTV on the inertial particles. After subtracting a pixel-wise minimum intensity background from each image, both phases are separated via an algorithm inspired by Khalitov & Longmire (2002). We set all pixels below a threshold intensity to zero, which we choose based on a visual inspection of each individual case. Contiguous groups of non-zero pixels are identified and labelled as either tracers or inertial particles contingent on their position in a size–intensity map. Pixels belonging to inertial particles are subtracted and substituted with a Gaussian noise of the same mean and standard deviation as the corresponding image. The resulting tracer-only images are then processed via a cross-correlation PIV algorithm with iterative window offset and deformation, applying one refinement step and 50 % overlap (Nemes *et al.* 2015). A Gaussian fitting function is used to determine sub-pixel displacements. Tests on synthetic images confirm that the cross-correlation algorithm accurately predicts

Focal length (mm)	Field of view ( $\text{cm}^2$ )	Field of view ( $L_{L,1}^2$ )	Resolution (pix $\text{mm}^{-1}$ )	PIV vector spacing (mm)	PIV vector spacing ( $\eta$ )
50	$30^2$	$2^2\text{--}3.3^2$	6	N/A	N/A
105	$12.5^2$	$0.8^2\text{--}1.6^2$	15	0.88–1.77	3.3–7.4
200	$4.5^2$	$0.3^2\text{--}0.6^2$	40	0.33–0.61	1.1–2.6

TABLE 3. Imaging parameters obtained with the CCD camera (2048 by 2048 pixels, 7.4  $\mu\text{m}$  pixel size) when mounting the different lenses. The large FOV with the 50 mm lens is not used for PIV.

tracer displacements within  $\pm 0.1$  pixels when their images are 2–3 pixels in size, representative of our small-FOV recordings. For the large and intermediate FOV, moderate peak locking is present in the distribution of particle displacements. This only marginally affects the fluid statistics in the present zero-mean-flow configuration, since the entire range of pixel displacement is associated with the turbulent motion (Carter *et al.* 2016). PIV vector validation is based on signal-to-noise ratio and deviation from the median of the neighbouring vectors (Westerweel & Scarano 2005). Non-valid vector percentages vary between experiments depending on camera resolution and inertial particle volume fraction. While most runs have fewer than 8 % of vectors rejected, the cases with higher particle concentration have 15–18 % rejected fluid velocity vectors. This is due to the background noise from light scattered by the ensemble of the inertial particles, rather than to the removal of individual particle images from local interrogation windows. Indeed, for the present cases, no statistical correlation is found between the location of non-valid vectors and the inertial particle position, except for the most highly concentrated cases where we do not attempt to extract fluid information. The dominant source of uncertainty on the flow statistics is the finite sample size, yielding typical uncertainties of 3 % for mean velocity measurements and 5 % for root mean square (r.m.s.) velocity fluctuations (Bendat & Piersol 2011).

The objects labelled as inertial particles are moved to a blank image and tracked via an in-house PTV algorithm. This is based on the cross-correlation approach (Hassan, Blanchat & Seeley 1992; Ohmi & Li 2000), although our version uses the full 12-bit pixel intensity information rather than the binarized image. The algorithm searches for a matching object within a specified radius around each particle centroid, maximizing the correlation coefficient between the image pairs. It performs well even with multiple neighbouring particles, since the local distribution pattern remains similar in the image pair. Mild peak locking is present in the large-FOV recordings of the smaller particles; however, as in the PIV of the tracers, the zero-mean-flow configuration limits the impact on the measured statistics. The process of phase separation is illustrated in figure 1, where a sample image is shown along with the resulting fluctuating velocity of flow tracers and inertial particles from PIV and PTV, respectively.

An advantage of the cross-correlation PTV approach is that its accuracy is weakly affected by the uncertainty in locating the object centroid. The latter will, however, affect the measurement of the particle spatial distribution, which is of interest in our study. We use different methods for locating the centroid, depending on the imaging conditions. For the larger FOV, the inertial particles cover typically 3–4 non-saturated pixels and a standard three-point Gaussian fit is appropriate. For the intermediate and small FOV, the particle images are larger and sometimes saturated.

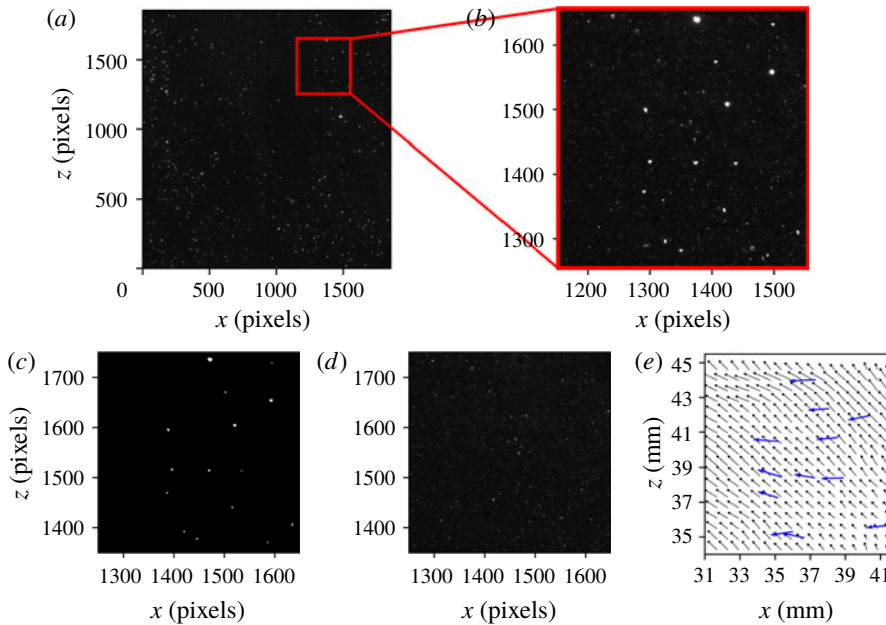


FIGURE 1. (Colour online) Image processing procedure for PIV/PTV measurements of tracer and particle motion: (a) raw image, (b) inset of raw image, (c) particle-only image, (d) tracer-only image, (e) resulting fluctuating fluid and particle velocity vectors.

In these cases, we use a least-squares Gaussian fit: for each object, a circular particle image of equivalent size is generated, following a Gaussian spatial distribution centred on the centre-of-mass of the original object (the weights being the pixel intensities). The position of the circular particle is then fitted to the original particle through a two-dimensional least-squares regression, yielding the sub-pixel centroid. The accuracy of both the three-point and least-squares methods has been tested on synthetic particle images with and without saturation. The least-squares method is more computationally expensive but more accurate, with an average error of 0.12 pixels in locating the centroid of saturated particles, against 0.45 pixels for the three-point fit. Importantly, the spatial distribution of particle count presents significant inhomogeneities only over the largest FOV, as shown in figure 2 for a representative case, which is due to the somewhat uneven laser illumination at those scales. This allows us to compute particle statistics via space–time ensemble averages over the full window, without the need to compensate for spatial gradients (Sumbekova *et al.* 2017).

Using our particle identification methods, we also are able to estimate the volume fraction  $\phi_v$ , by counting the number of particles in the FOV and comparing their total volume with the illuminated volume. Even at the higher loading considered, the average inter-particle distance is at least  $\sim 1$  mm, which is larger than the particle image. Due to clustering, particles may be found much closer to each other, preventing their individual identification. However, intense clustering usually pertains to a limited fraction of the particle set (Baker *et al.* 2017), and thus the number of undetected ones is expected to be relatively small. Yang & Shy (2005) and recently Sahu *et al.* (2014, 2016) carried out experiments in similar conditions and used the same approach to estimate  $\phi_v$ . This method has proven robust also in our recent study of a particle-laden channel flow, in which we imaged 50  $\mu\text{m}$  glass beads at  $\phi_v = O(10^{-5})$  with a similar

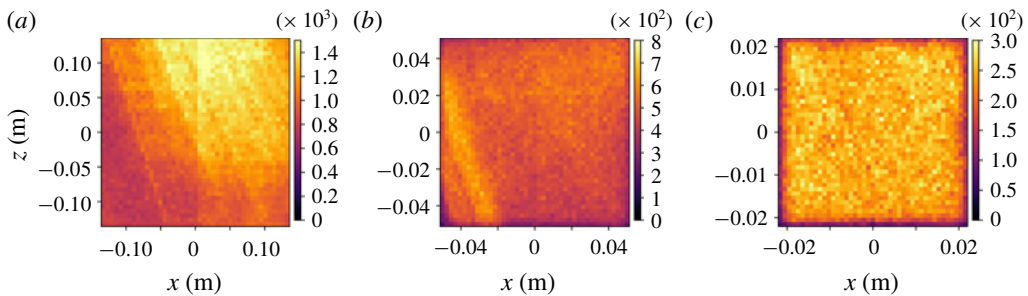


FIGURE 2. (Colour online) Particle counts for example FOVs.

PIV system (Coletti *et al.* 2016; Nemes *et al.* 2016). In that case the imaging-based volume fraction agreed to within 12–15 % the value obtained from the amount of particles accumulated in the exit plenum during a given run time.

### 2.3. Voronoï tessellation and cluster identification

To analyse the spatial distribution and concentration of the inertial particles, and in particular the properties of discrete clusters, we make use of the Voronoï diagram method (Monchaux, Bourgoin & Cartellier 2010). This approach divides the domain (in this case, the two-dimensional image) into a tessellation of cells associated with individual particles, each cell containing the set of points closer to that particle than to any other. The inverse of the area  $A$  of each cell equals the local particle concentration,  $C = 1/A$ . The method has been used to analyse particle-laden turbulent flows in both experimental (Obligado *et al.* 2014; Rabencov & van Hout 2015; Sumbekova *et al.* 2017) and numerical studies (Tagawa *et al.* 2012; Dejoan & Monchaux 2013; Kidanemariam *et al.* 2013; Frankel *et al.* 2016; Zamansky *et al.* 2016; Baker *et al.* 2017; Monchaux & Dejoan 2017). Figure 3(a) shows the Voronoï tessellation for one small-FOV realization, and a representative probability density function (PDF) of cell areas normalized by the mean value  $\langle A \rangle$  is plotted in figure 3(b). (Here and in the following, angle brackets denote ensemble average.) As typical for clustered particle fields, the observed PDF is much wider than that of a random Poisson process, which follows a  $\Gamma$  distribution (Ferenc & Néda 2007). Figure 3(c) shows the centred and normalized PDFs of the logarithm of the Voronoï cell areas for all our experiments, indicating a reasonable collapse that emphasizes their quasi-lognormality. This behaviour has been exploited to characterize the particle distribution by a single parameter, the standard deviation  $\sigma_A$  (Monchaux *et al.* 2010).

The value  $A^*$ , below which the probability of finding sub-average cell areas is higher than in a Poisson process, is usually taken as the threshold for particles to be considered clustered (Monchaux *et al.* 2010; Rabencov & van Hout 2015; Sumbekova *et al.* 2017, among others). Individual clusters are then defined as connected groups of such particles, as shown in figure 3(a). To avoid spurious edge effects, we apply the additional constraint that the area of all neighbouring cells are also smaller than  $A^*$  (a condition first introduced by Zamansky *et al.* (2016)). Figure 3(d) shows the PDFs of cluster areas  $A_C$  for a representative case, obtained with and without this latter condition. Such a condition separates objects connected by only one Voronoï cell. The edge effect produces ripples in the distribution without the neighbour cell condition, indicating that certain cluster sizes are unlikely to occur, possibly due to

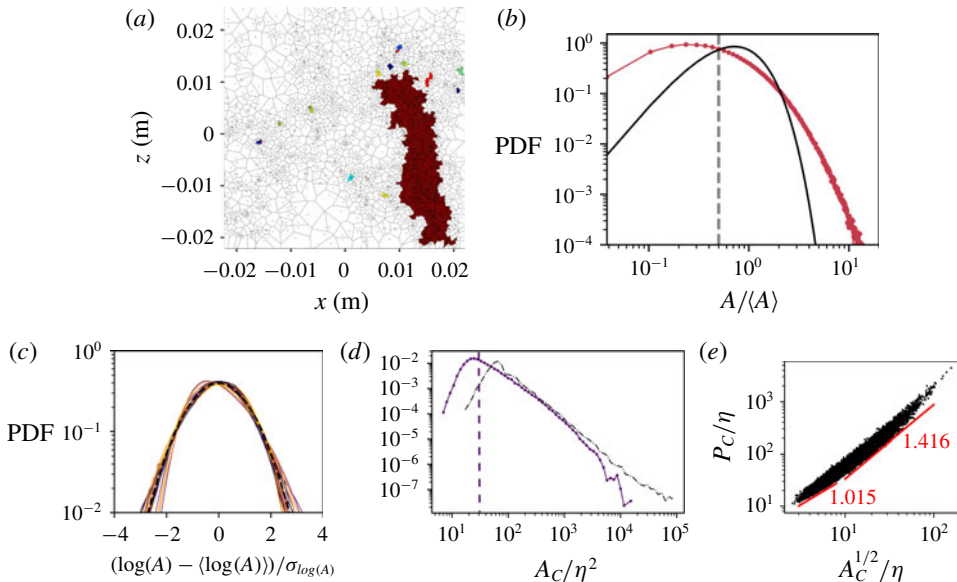


FIGURE 3. (Colour online) (a) Example Voronoï tessellation with connected sets of Voronoï cells below the area threshold coloured. (b) Example Voronoï area PDF shows clear departure from random Poisson distribution indicating the presence of clusters and voids for a case with  $St_\eta = 3.2$ . (c) All PDFs of  $\log(A)$ , centred at the mean and normalized by the standard deviation. The black dotted line shows a normal distribution with variance = 1. (d) PDF of a sample case, with (purple circles) and without (black dashes) the neighbouring cell condition. (e) Scatter plot of cluster perimeter and square root of its area (same case as in d).

the coagulation of neighbouring connected objects; the application of the neighbouring cell condition removes this artefact. This allows us to isolate very small clusters and to separate artificially large ones; hence the apparent shift in the area PDF.

Following Baker *et al.* (2017), we use the Voronoï diagram method to identify individual clusters, focusing on those sufficiently large to exhibit a scale-invariant structure. Figure 3(e) displays, for the same case as in figure 3(d), the scatter plot of cluster perimeters ( $P_C$ ) versus the square root of their areas ( $A_C^{1/2}$ ). (We refer to cluster perimeter and cluster area, although these are strictly properties of the connected set of Voronoï cells associated with the particles in each cluster, rather than to the cluster itself.) For small clusters, the data points follow a power law with exponent  $\sim 1$  as expected for regular two-dimensional objects, while for larger ones the exponent is approximately 1.4, indicating a convoluted structure of the cluster borders. This trend, common to all our experiments, was observed in several previous studies (e.g. Monchaux *et al.* 2010; Rabencov & van Hout 2015; Baker *et al.* 2017) using Voronoï tessellation, and earlier Aliseda *et al.* (2002) using box-counting), and is consistent with the view of inertial particle clusters as fractal sets (Bec 2003; Bec *et al.* 2007; Calzavarini *et al.* 2008), although it must be remarked that this latter feature was shown to be associated with the dissipative scales. The minimum size for the emergence of fractal clustering is difficult to identify precisely in figure 3(e); however, as shown by Baker *et al.* (2017), this also corresponds to the emergence of self-similarity of the cluster sizes, as indicated by the power-law decay in their

size distribution. This threshold can be located with more confidence in figure 3(d) (dashed line); it is taken as the condition for a cluster to be coherent, i.e. associated with the coherent motions in the underlying turbulent field rather than by accidental particle proximity (Baker *et al.* 2017).

#### 2.4. Parameter space

Table 4 reports the main physical parameters and imaging resolution for all experimental runs, 57 in total. Not all cases are used for all types of analysis: for example, the glass bubbles are very light and do not allow sufficiently accurate measurements of the settling velocity, while the 100  $\mu\text{m}$  glass beads do not disperse homogeneously enough to perform clustering analysis. The importance of particle weight is characterized by the settling parameter  $Sv_\eta = W_0/u_\eta$ , where  $u_\eta = \eta/\tau_\eta$  is the Kolmogorov velocity. Since both small-scale and large-scale eddies are consequential for the settling process, a definition based on the r.m.s. fluid velocity fluctuation,  $Sv_L = W_0/u'$ , is also relevant (Good *et al.* 2014). The Froude number  $Fr = St_\eta/Sv_\eta$  is also often used in the literature, and is reported in table 4 for completeness. From a comparison with previous studies, we expect the turbulence to induce significant clustering and settling modification, and the particles to possibly modify the turbulence at the higher volume fractions. We remark that, as in any laboratory study with a fixed gravitational acceleration, varying only one parameter at a time is not feasible. For example, increasing  $St_\eta$  by using heavier particles leads to higher  $Sv_\eta$ , unless  $Re_\lambda$  is also adjusted. Likewise, varying  $\phi_v$  may modify the turbulence properties, and therefore the effective values of the other parameters. Therefore, throughout the paper we will often show the simultaneous dependence of the observables with multiple parameters.

### 3. Particle spatial distribution

#### 3.1. Particle fields

In this section we explore the spatial structure of the inertial particle fields and the length scales over which clustering occurs. In the literature this has been characterized by two main tools: the radial distribution function (RDF) and, more recently, Voronoï tessellation. Both methods provide different and complementary information – we apply them both for a comprehensive description.

The RDF describes the scale-by-scale concentration in the space surrounding a generic particle, compared to a uniform distribution. For 2-D distributions such as those obtained by planar imaging, this is defined as:

$$g(r) = \frac{N_r/A_r}{N/A_{tot}}, \quad (3.1)$$

where  $N_r$  represents the number of particles within an annulus of area  $A_r$ , while  $N$  is the total number of particles within the planar domain of area  $A_{tot}$ . In the presence of clustering, the RDF is expected to increase for decreasing  $r$ , and the range over which it remains greater than unity indicates the length scale over which clustering occurs (e.g. Sundaram & Collins 1997; Reade & Collins 2000; Wood, Hwang & Eaton 2005; Saw *et al.* 2008; de Jong *et al.* 2010; Ireland *et al.* 2016*a,b*). We compute RDFs by binning particle pairs based on their separation distance. To avoid projection biases at separations below the illuminated volume thickness (Holtzer & Collins 2002), we only

Case	Material	$Re_\lambda$	$d_p/\eta$	$St_\eta$	$Sv_\eta$	$Sv_L$	$Fr$	$\phi_v$	$\phi_m$
1	Glass	500	0.52	20.8	5.6	0.59	3.7	$5.5 \times 10^{-5}$	$1.0 \times 10^{-1}$
2	Glass	500	0.43	14.7	6.5	0.66	2.3	$2.6 \times 10^{-6}$	$5.3 \times 10^{-3}$
3	Glass	300	0.43	14.0	6.8	0.77	2.1	$3.4 \times 10^{-5}$	$6.9 \times 10^{-2}$
4	Glass	500	0.42	14.0	6.7	0.66	2.1	$2.5 \times 10^{-6}$	$5.2 \times 10^{-3}$
5	Glass	500	0.40	12.4	7.1	0.63	1.8	$1.5 \times 10^{-5}$	$3.1 \times 10^{-2}$
6	Glass	500	0.40	12.4	7.1	0.63	1.8	$1.6 \times 10^{-5}$	$3.7 \times 10^{-2}$
7	Glass	300	0.40	12.5	7.1	0.90	1.8	$1.6 \times 10^{-6}$	$3.4 \times 10^{-3}$
8	Glass	300	0.39	12.0	7.2	0.86	1.7	$1.7 \times 10^{-6}$	$3.8 \times 10^{-3}$
9	Glass	300	0.35	9.8	8.0	0.77	1.2	$1.7 \times 10^{-5}$	$3.5 \times 10^{-2}$
10	Glass	500	0.26	6.5	2.3	0.24	2.9	$6.5 \times 10^{-6}$	$1.3 \times 10^{-2}$
11	Glass	500	0.26	6.6	2.3	0.23	2.7	$3.2 \times 10^{-7}$	$6.5 \times 10^{-4}$
12	Glass	400	0.26	6.4	2.3	0.26	2.8	$2.4 \times 10^{-7}$	$4.9 \times 10^{-4}$
13	Glass	500	0.24	5.8	2.3	0.23	2.5	$1.2 \times 10^{-6}$	$2.4 \times 10^{-3}$
14	Glass	500	0.24	5.4	2.4	0.24	2.2	$9.5 \times 10^{-7}$	$1.9 \times 10^{-3}$
15	Glass	500	0.23	5.2	2.5	0.23	2.1	$1.4 \times 10^{-6}$	$2.8 \times 10^{-3}$
16	Glass	500	0.23	5.1	2.6	0.25	2.0	$1.4 \times 10^{-7}$	$2.9 \times 10^{-4}$
17	Glass	300	0.23	5.1	2.5	0.30	2.0	$3.6 \times 10^{-7}$	$7.4 \times 10^{-4}$
18	Glass	300	0.23	4.9	2.6	0.31	1.9	$2.2 \times 10^{-5}$	$4.6 \times 10^{-2}$
19	Glass	500	0.22	4.6	2.6	0.23	1.8	$2.3 \times 10^{-6}$	$4.8 \times 10^{-3}$
20	Glass	500	0.22	4.6	2.6	0.23	1.8	$6.6 \times 10^{-7}$	$1.3 \times 10^{-3}$
21	Glass	500	0.22	4.6	2.6	0.23	1.8	$2.8 \times 10^{-5}$	$5.7 \times 10^{-2}$
22	Glass	500	0.21	4.4	2.7	0.26	1.7	$3.1 \times 10^{-6}$	$6.3 \times 10^{-3}$
23	Glass	300	0.21	4.2	2.7	0.34	1.5	$2.3 \times 10^{-6}$	$4.8 \times 10^{-3}$
24	Glass	300	0.21	4.6	2.6	0.28	1.7	$1.8 \times 10^{-6}$	$3.8 \times 10^{-3}$
25	Glass	500	0.20	4.1	2.7	0.30	1.5	$6.6 \times 10^{-8}$	$1.4 \times 10^{-4}$
26	Glass	300	0.20	4.1	2.8	0.34	1.5	$1.0 \times 10^{-6}$	$2.0 \times 10^{-3}$
27	Glass	300	0.19	3.6	2.9	0.29	1.2	$6.5 \times 10^{-6}$	$1.3 \times 10^{-2}$
28	Glass	300	0.19	3.6	2.9	0.29	1.2	$3.8 \times 10^{-6}$	$7.8 \times 10^{-3}$
29	Glass	300	0.19	3.2	3.3	0.38	1.0	$2.3 \times 10^{-7}$	$4.7 \times 10^{-4}$
30	Glass	300	0.18	3.3	3.0	0.39	1.0	$1.6 \times 10^{-7}$	$3.2 \times 10^{-4}$
31	Glass	500	0.15	2.8	1.0	0.10	2.9	$4.8 \times 10^{-7}$	$9.8 \times 10^{-4}$
32	Glass	500	0.15	3.2	0.90	0.10	3.5	$3.0 \times 10^{-7}$	$6.2 \times 10^{-4}$
33	Glass	500	0.15	2.9	1.0	0.10	3.0	$4.4 \times 10^{-8}$	$9.0 \times 10^{-5}$
34	Glass	300	0.14	2.4	1.1	0.13	2.2	$8.0 \times 10^{-8}$	$1.6 \times 10^{-4}$
35	Glass	500	0.13	2.4	1.0	0.10	2.3	$8.0 \times 10^{-8}$	$1.6 \times 10^{-4}$
36	Glass	300	0.13	2.2	1.1	0.13	2.0	$4.2 \times 10^{-7}$	$8.5 \times 10^{-4}$
37	Glass	500	0.12	2.0	1.1	0.10	1.8	$5.8 \times 10^{-7}$	$1.2 \times 10^{-3}$
38	Glass	500	0.12	2.0	1.1	0.10	1.8	$2.7 \times 10^{-8}$	$5.0 \times 10^{-5}$
39	Glass	500	0.12	2.0	1.1	0.10	1.8	$2.6 \times 10^{-6}$	$5.3 \times 10^{-3}$
40	Glass	500	0.12	2.0	1.1	0.10	1.8	$1.2 \times 10^{-7}$	$2.4 \times 10^{-4}$
41	Glass	300	0.12	2.0	1.1	0.13	1.7	$6.3 \times 10^{-7}$	$1.3 \times 10^{-3}$
42	Glass	300	0.12	1.8	1.2	0.14	1.6	$8.4 \times 10^{-7}$	$1.7 \times 10^{-3}$
43	Glass	300	0.11	1.6	1.3	0.12	1.2	$7.8 \times 10^{-7}$	$1.6 \times 10^{-3}$
44	Glass	300	0.11	1.7	1.2	0.14	1.4	$8.8 \times 10^{-7}$	$1.8 \times 10^{-3}$
45	Glass	300	0.11	1.7	1.2	0.15	1.4	$1.4 \times 10^{-7}$	$2.8 \times 10^{-4}$
46	Glass	300	0.11	1.6	1.3	0.12	1.2	$2.1 \times 10^{-6}$	$4.4 \times 10^{-3}$
47	Glass	300	0.11	1.8	1.2	0.14	1.5	$6.5 \times 10^{-8}$	$1.3 \times 10^{-4}$
48	Glass	300	0.11	1.6	1.3	0.13	1.2	$6.7 \times 10^{-8}$	$1.4 \times 10^{-4}$
49	Glass	300	0.11	1.7	1.2	0.14	1.4	$1.3 \times 10^{-7}$	$2.7 \times 10^{-4}$
50	Glass	200	0.09	1.1	1.6	0.22	0.73	$1.2 \times 10^{-7}$	$2.4 \times 10^{-4}$

TABLE 4. (continued)

51	Lycopodium	500	0.12	0.80	0.46	0.04	1.8	$5.4 \times 10^{-7}$	$5.3 \times 10^{-4}$
52	Lycopodium	500	0.12	0.80	0.46	0.04	1.8	$8.6 \times 10^{-8}$	$8.0 \times 10^{-5}$
53	Lycopodium	300	0.12	0.75	0.48	0.06	1.6	$1.6 \times 10^{-7}$	$5.0 \times 10^{-4}$
54	Lycopodium	300	0.11	0.63	0.51	0.05	1.2	$9.4 \times 10^{-6}$	$9.2 \times 10^{-3}$
55	Lycopodium	300	0.11	0.63	0.51	0.05	1.2	$6.0 \times 10^{-7}$	$5.9 \times 10^{-4}$
56	Lycopodium	300	0.11	0.63	0.51	0.05	1.2	$1.9 \times 10^{-7}$	$1.8 \times 10^{-4}$
57	Glass bubbles	300	0.34	0.37	0.30	0.03	1.2	$3.4 \times 10^{-5}$	$2.7 \times 10^{-3}$

TABLE 4. Main experimental parameters for all considered cases, ordered in decreasing particle Stokers number  $St_\eta$ .

calculate  $g(r)$  for  $r > 1.5$  mm. As noted by de Jong *et al.* (2010), imaging-based RDF measurements are sensitive to the size and shape of the observation region, and some sort of edge-correction strategy is needed for particles near the image boundaries. One can omit statistics for radial annuli that cross the image boundary, but this approach has two shortcomings: the maximum separation becomes limited to the radius of the domain-inscribed circle; and the number of particle pairs per unit area used to calculate the RDF decreases as the separation increases. Both effects combine to thwart the reliable assessment of large-scale clustering. Indeed, past RDF measurements at distances  $O(L)$  in flows with wide scale separation were obtained using single-point probes and invoking Taylor's hypothesis (Saw *et al.* 2008, 2012; Bateson & Aliseda 2012). Here, following de Jong *et al.* (2010), we leverage the spatial homogeneity of our fields and apply a periodic-domain correction: the particle field is mirrored across the image boundaries, so that the same number of radial annuli can be used for each particle location, yielding a maximum separation equal to the full size of the FOV. Although this assumption introduces unphysical correlations between particles near the reflected boundaries, numerical experiments using DNS showed the associated error to be small (Salazar *et al.* 2008).

Due to the large range of scales separation ( $L/\eta \sim O(10^3)$ ,  $L/d_p \sim O(10^4\text{--}10^5)$ ) it is not feasible to simultaneously resolve all scales at play, and thus the small-FOV and large-FOV imaging will suffer from large-scale and small-scale cutoffs, respectively. Comparing the different FOVs, however, provides quantitative information over a wide range of scales. Figure 5(a) shows examples from the small-FOV measurements. At small separations, several authors have found satisfactory fit to the data using a power law, which indicates a self-similar spatial distribution (Chun *et al.* 2005; Salazar *et al.* 2008; Zaichik & Alipchenkov 2009; Ireland *et al.* 2016a,b):

$$g(r/\eta) = c_0(r/\eta)^{-c_1}, \quad (3.2)$$

where  $c_0$  and  $c_1$  are coefficients dependent on  $St_\eta$  (and, in presence of gravity,  $Sv_\eta$ ). While theoretical arguments consistent with this formulation strictly apply for dissipative separations ( $r/\eta < 1$ , Chun *et al.* (2005) and Saw *et al.* (2008) argued that the power-law form should continue into the correlation scale of the velocity gradients ( $r/\eta = O(10)$ ). In figure 4(a) we see indeed that RDFs closely follow a power-law decay up to  $r/\eta \approx 40$  for  $St_\eta$  close to unity. The departure from the power law at larger separations indicates the particle set is not self-similar at those scales (Bragg, Ireland & Collins 2015). We evaluate the coefficients  $c_0$  and  $c_1$  by least-square fits over the range  $10 < r/\eta < 30$ , and plot them in figure 4(b,c) as a function of  $St_\eta$ . The error bars for the coefficients comes from the covariance matrix of the fit. The results,

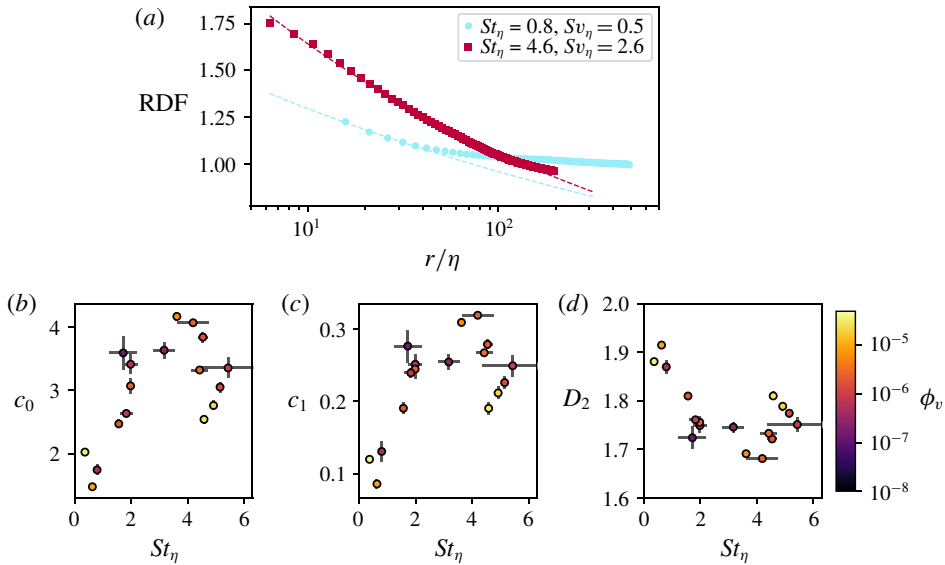


FIGURE 4. (Colour online) (a) Example RDFs where symbols represent the calculated RDFs and dashed lines their fits according to (3.2). Panels (b,c) show the fitted values versus  $St_\eta$ , and (d) shows the value of the correlation dimension.

which are only weakly sensitive to varying the fit upper bound between  $r/\eta = 20$  and 40, display the higher values in the approximate range  $1.5 < St_\eta < 4$ . This confirms that particles with Stokes number  $O(1)$  display the stronger degree of clustering over the near-dissipative range. However, the most intense clustering occurs for  $St_\eta > 1$ , possibly because of the significant effect of gravitational settling as discussed below. The trend and values are in fair quantitative agreement with the DNS of Ireland *et al.* (2016b) in similar conditions. The  $c_1$  coefficient is related to the correlation dimension used in dynamical system theory (Bec *et al.* 2008),  $D_2 = n - c_1$ , where the number of spatial dimensions is  $n = 2$  for our planar realizations. Figure 5(d) plots  $D_2$  for the different cases, showing trends and values consistent with the channel flow experiments by Fessler *et al.* (1994) and the grid turbulence experiments by Monchaux *et al.* (2010, 2012). For increasing particle inertia, one expects a loss of spatial correlation as the particle response time grows beyond the fine turbulent scales. Although the present range does not extend to very large  $St_\eta$ , we note that the return to a homogeneous distribution appears slow. Recent numerical studies compared settling and non-settling conditions, and concluded that gravity hinders clustering for  $St_\eta < 1$  but enhances it for  $St_\eta > 1$ , resulting in significant clustering over a wide range of Stokes numbers (Bec, Homann & Ray 2014b; Gustavsson, Vajedi & Mehlig 2014; Ireland *et al.* 2016b; Baker *et al.* 2017; Matsude, Onishi & Takahashi 2017). Ireland *et al.* (2016b) attributed this behaviour to the competing effects of the particle path history and preferential flow sampling. Sahu *et al.* (2016) measured RDFs for spray droplets and also noticed an increasing tendency to cluster for increasing  $St_\eta$  (although their range was very close to unity).

The large-FOV measurements allow us to probe the spatial distribution over much greater scales. Figure 5(a) clearly indicates that considerable clustering occurs over lengths  $O(L)$ . For a quantitative assessment, we consider the original power-law model

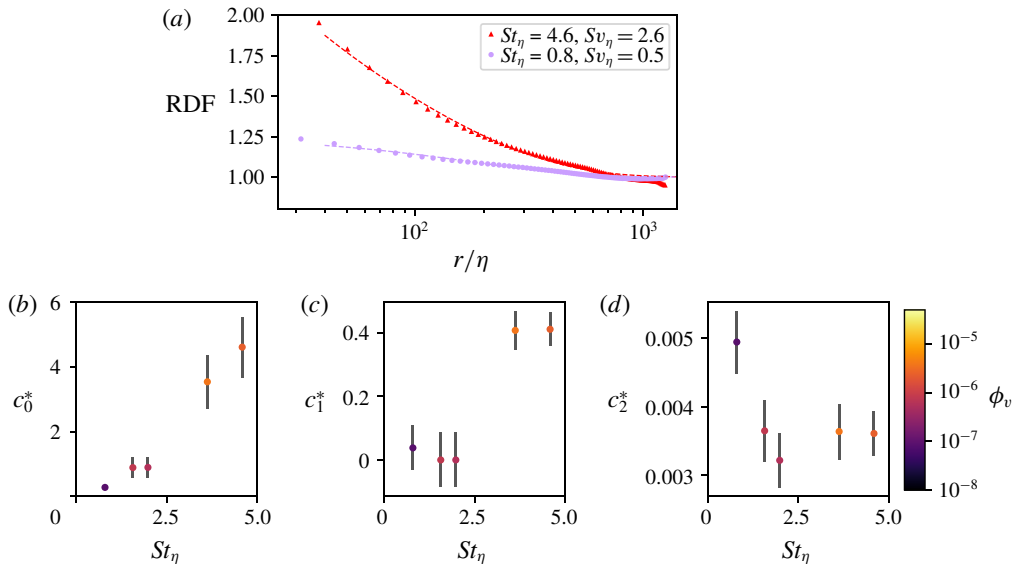


FIGURE 5. (Colour online) (a) Example RDFs where symbols represent the calculated RDFs and dashed lines their fits according to (3.3). Panels (b–d) show the fitted coefficients versus  $St_\eta$ .

proposed by Reade & Collins (2000):

$$g(r/\eta) - 1 = c_0^*(r/\eta)^{-c_1^*} e^{-c_2^* r/\eta}, \quad (3.3)$$

which, unlike (3.2), does recover the return to unity at large separations. The excellent fit to the data over the entire window confirms the observation made by Reade & Collins (2000), that the RDFs of preferentially concentrated particles have a power-law decay at small scales and an exponential tail at large scales. Figure 5(b–d) displays the least-square-fit coefficients as a function of  $St_\eta$ . The  $c_2^*$  coefficient decreases as  $St_\eta$  increases, implying a greater spatial extent of clustering for the more inertial particles. This may be due to the more inertial particles responding to larger time scales of the turbulence, and to the influence of gravitational settling as mentioned above. The length scale of the large-scale clustering can be estimated from the exponential decay as  $\eta/c_2$ , which for  $St_\eta > 1$  is approximately  $300\eta$ – $400\eta$ , close to the integral scale of the turbulence. Taken together, these results confirm that clustering can extend over larger scales for heavier particles. This is in agreement with the conceptual picture of Goto & Vassilicos (2006) and Yoshimoto & Goto (2007) and the simulations of Bec *et al.* (2010) and Ireland *et al.* (2016*a,b*), which showed that particles of  $St_\eta > 1$  respond to eddies in the inertial range. However, as we will reiterate in the next sub-section, the present results indicate that some level of clustering may extend even beyond, approaching the integral scales.

The degree of clustering can also be evaluated from the Voronoï diagrams. We remark that the type of information provided by this method is somewhat different than the RDF. The latter is strictly a two-particle quantity, while the shape and size of the Voronoï cells result from the mutual position of multiple particles. Therefore, we look for an insight complementary to our RDF results. In figure 6(*a*) we plot the standard deviation of the Voronoï cell areas  $\sigma_A$  as a function of the Stokes number,

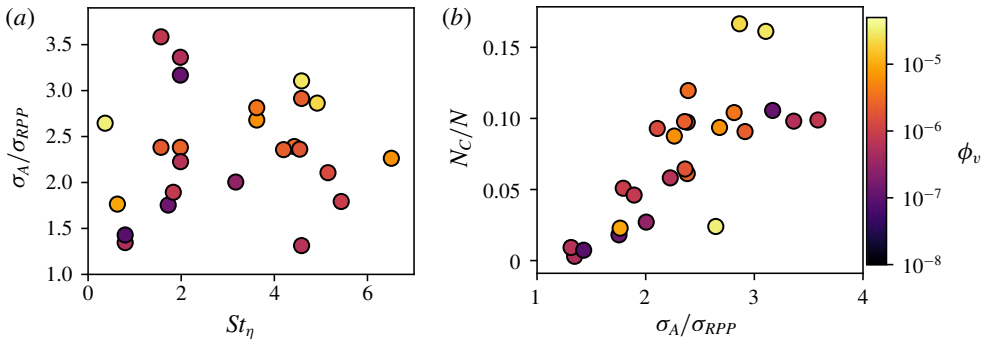


FIGURE 6. (Colour online) Two qualifications of clustering intensity using the Voronoi tessellation method: (a)  $\sigma_A/\sigma_{RPP}$  representing departure from a random particle distribution versus Stokes number. (b) Fraction of inertial particles belonging to coherent clusters as a function of normalized  $\sigma_A/\sigma_{RPP}$ .

normalizing it by the expected value for particles distributed according to a random Poisson process,  $\sigma_{RPP} \approx 0.53$  (Monchaux *et al.* 2010). As a general trend, clustering is most pronounced for particles of  $St_\eta \approx 1$ , in agreement with previous studies (Monchaux *et al.* 2010; Tagawa *et al.* 2012; Dejoan & Monchaux 2013; Monchaux & Dejoan 2017). However, the significant scatter suggests that other parameters may also play a role. Indeed, in their grid turbulence study, Sumbekova *et al.* (2017) found that  $\sigma_A$  was strongly dependent on  $Re_\lambda$ , moderately on  $\phi_v$  and negligibly on  $St_\eta$ . While the considerable degree of polydispersity in their experiments may have influenced such conclusion, their results convincingly indicated that clustering is affected by a range of turbulent scales, whose breadth is controlled by  $Re_\lambda$ . Moreover, as pointed out by Baker *et al.* (2017),  $\sigma_A$  is not only a function of the concentration of the clustered particles, but also of the size and distribution of the voids, and the latter are strongly influenced by the inertial and integral scales of the turbulence (Yoshimoto & Goto 2007).

The decrease in  $\sigma_A$  for  $St_\eta > 1$  is mild. Since increasing  $St_\eta$  also implies increasing  $Sv_\eta$ , this again suggests that, in this range, gravitational settling may enhance clustering. This idea is supported by figure 6(b), showing the fraction of particles belonging to coherent clusters (according to the definition in § 2.3) plotted versus  $\sigma_A$ . A clear correlation is visible, indicating that the number of clustered particles,  $N_c$ , is similarly affected by the physical parameters. The values are possibly underestimated, because particles in highly concentrated regions are more likely to be overshadowed by neighbouring particles and go undetected. Still, the results are in fair agreement with the DNS of Baker *et al.* (2017), where less than 3% of the particles with  $St_\eta < 1$  belonged to coherent clusters, with the percentage increasing up to 14% for  $St_\eta = O(10)$ . Therefore, the more inertial (and faster falling) particles are more likely to belong to clusters; or, equivalently, they tend to form clusters that are more numerous, larger, or denser. The question of the cluster size and the concentration within them is addressed in the following section.

### 3.2. Individual clusters

The multi-scale nature of the clustering process is reflected in the features of the individual clusters. Figure 7 shows several sample clusters from various instantaneous

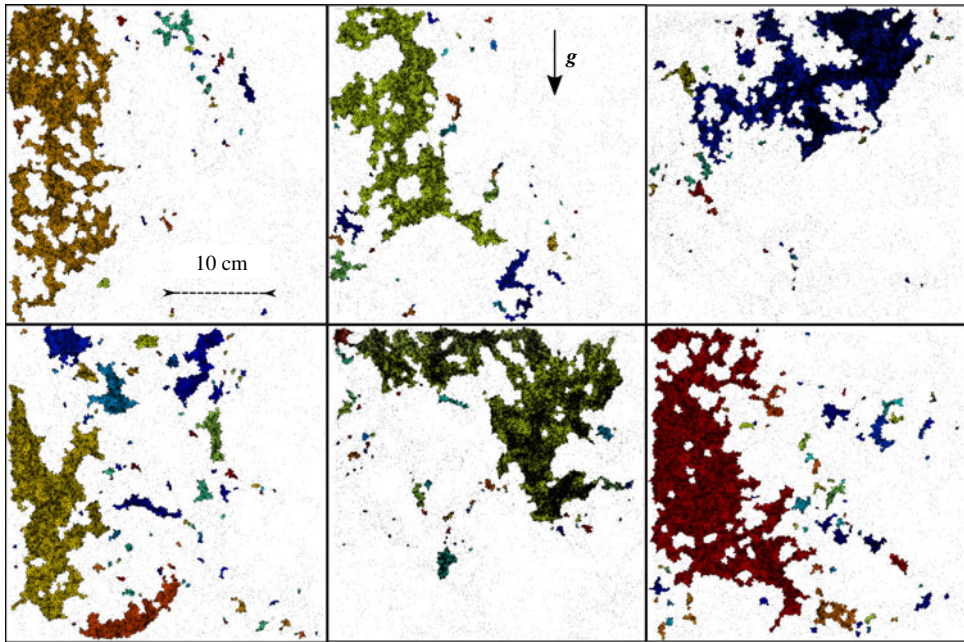


FIGURE 7. (Colour online) Example clusters for the cases  $St_\eta = 1.6$  and  $4.6$  imaged in the large FOV, highlighting the wide variety of sizes and shapes.

realizations, as captured by the large-FOV measurements and identified by the Voronoi diagram method, illustrating the variety of sizes and complex shapes of these objects. Some of them are even larger than the integral scales of the flow, often exceeding the limits of the imaging window. Their borders are jagged and convoluted, and their bodies non-simply connected. In the following, we provide quantitative support to these observations. We stress that the objects captured by 2-D imaging are cross-sections of 3-D clusters; this naturally conditions our ability to assess their topology. Such limitation, however, is not expected to overshadow the main conclusions of the analysis.

Figure 8 shows the PDFs of the areas  $A_C$  of the clusters, coherent and not, distinguishing between measurements obtained over the small, intermediate and large FOV. In agreement with Baker *et al.* (2017) and Sumbekova *et al.* (2017), most cases display a power-law behaviour over several decades, suggesting a self-similar hierarchy of structures, possibly associated with the scale-invariant properties of the underlying turbulent field (Moisy & Jiménez 2004; Goto & Vassilicos 2006). The data are consistent with the previously suggested values of  $-2$  and  $-5/3$  for the power-law exponent for planar measurements (Monchaux *et al.* 2010; Obligado *et al.* 2014; Sumbekova *et al.* 2017).

As expected, the spatial resolution influences the size distributions. The small FOV is affected by a cutoff at large scales. At small scales, the limited resolution in the large FOV makes particles more likely to go undetected due to the glare of their neighbours, reducing the probability of finding small clusters. The latter effect can partly explain why the area threshold for self-similarity (see vertical dashed line in figure 3d) varies significantly between cases, while this was found to be very consistent in the simulations of Baker *et al.* (2017). Another factor influencing

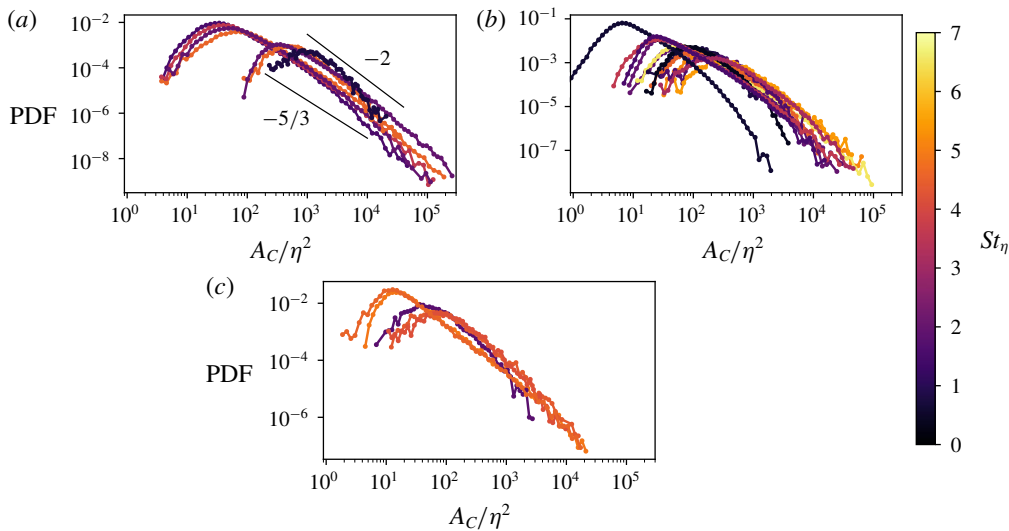


FIGURE 8. (Colour online) PDFs of cluster area normalized by  $\eta$  and separated by FOV size. Largest FOV ( $30 \times 30 \text{ cm}^2$ ) is shown in (a), medium field ( $14.5 \times 14.5 \text{ cm}^2$ ) in (b) and smallest field in (c) ( $4.5 \times 4.5 \text{ cm}^2$ ).

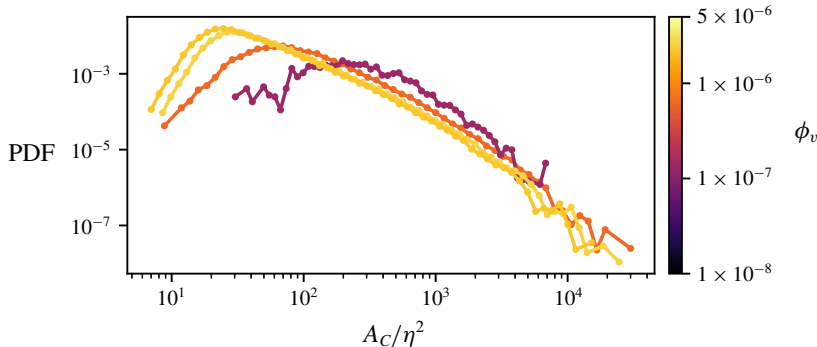


FIGURE 9. (Colour online) PDFs of cluster area for experiments with  $St_\eta$  between 1 and 2.5 ( $30 \mu\text{m}$  glass spheres) in the medium FOV showing how increasing volume fraction shifts PDFs to smaller scales.

this threshold is the particle volume fraction. Although the value of  $A^*$  was shown to be robust to particle sub-sampling (Monchaux *et al.* 2012; Baker *et al.* 2017), varying the number of particles in the domain results in a shift of the cluster area distribution (figure 9), which in turn affects the number of detected coherent clusters above the self-similar threshold. Finally, as  $\phi_v$  increases, the possibility of significant two-way coupling effects also increases, which may alter the turbulence structure and consequently the clustering process. This aspect will be discussed in § 5.5.

A remarkable aspect of the distributions in figure 8 is the non-negligible probability of finding clusters of size comparable to the inertial scales of the turbulence. Since our definition of coherent clusters entails a power-law size distribution, and this is found to have an exponent close to  $-2$ , the mean area of the coherent clusters is

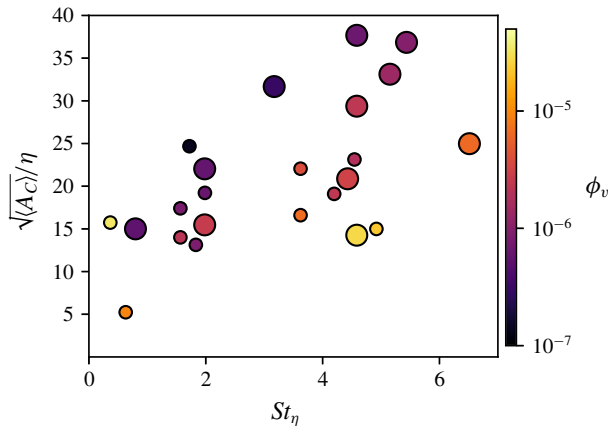


FIGURE 10. (Colour online) Mean cluster area versus particle inertia. Marker size is proportional to  $Re_\lambda$  of the underlying turbulent flow.

ill defined. In order to compare with past studies, we calculate the mean area of all clusters  $\langle A_C \rangle$ , below and above the self-similarity threshold, and plot its square root in figure 10. The majority of cases display mean sizes between  $10\eta$  and  $40\eta$ , with a generally increasing trend with  $St_\eta$ . Several previous studies have reported mean cluster sizes around  $10\eta$  (Aliseda *et al.* 2002; Wood *et al.* 2005; Dejoan & Monchaux 2013). Most of these studies, however, considered turbulent flows with relatively low  $Re_\lambda$  and thus limited scale separation. Recently, Sumbekova *et al.* (2017) investigated droplets in grid turbulence at  $Re_\lambda$  approaching 500, and found cluster size distributions and averages comparable with ours. At large Reynolds numbers the spectrum of temporal scales widens, and particles with a broad range of response times become susceptible to clustering mechanisms (Yoshimoto & Goto 2007). As noted in § 3.2, the more inertial particles respond to larger eddies and therefore can agglomerate in larger sets. The observed dependence of the cluster size with  $St_\eta$  is consistent with this view.

To investigate the degree of self-similarity exhibited by individual clusters, and to provide a descriptor of their complex shape, we calculate their box-counting dimension. This has been widely used to characterize the topology of both turbulent structures (Moisy & Jiménez 2004; Lozano-Durán, Flores & Jiménez 2012; Carter & Coletti 2018) and particle clusters in turbulence (Baker *et al.* 2017). The domain is partitioned into non-overlapping square boxes of side length  $r$ , and for each cluster we count the number of boxes  $N_B$  containing at least one particle. If  $N_B(r)$  follows a power law, i.e.  $N_B \sim r^{-D}$ , over a sizable range of scales, the exponent  $D$  is taken as the box-counting dimension of the object, which is in turn a measure of its fractal dimension. (Several other definitions of fractal dimension exist, and typically they only coincide for mathematical constructs, Falconer (2003).) Relatively large objects are needed for a robust estimate of  $D$  over a wide range of scales, and we thus consider only clusters of area larger than  $10^4\eta^2$ . Additionally, we neglect clusters touching the image boundary, as their silhouette would include spurious straight segments. Figure 11 shows, for three sample cases,  $N_B(r)$  normalized by the maximum number of boxes for each cluster (corresponding to the smallest box size,  $r = \eta$ ). For each case, curves for only 20 example clusters are shown for clarity. These reveal a remarkably consistent box-counting dimension  $D \approx 1.6$  over at least a

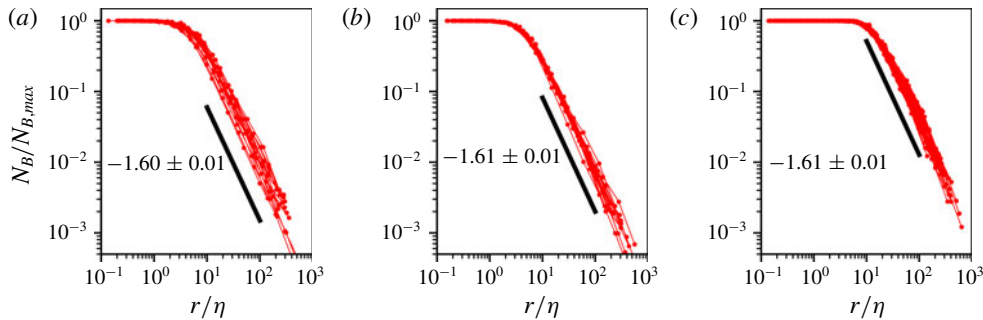


FIGURE 11. (Colour online)  $N_B(r)$  for three cases with  $St_\eta = 4.6$  in (a), 3.6 in (b) and 2.0 in (c), normalized by the respective maximum. The box-counting dimension of 1.6 is consistent for all cases.

decade of scales; the same trend is followed by all other cases. Baker *et al.* (2017) found  $D \approx 1.9$  for 3-D clusters. Relating the box-counting dimension of 3-D objects and their 2-D cross-sections is not straightforward (Tang & Marangoni 2006; Carter & Coletti 2018). Rather, the present result may be compared with that of Carter & Coletti (2018) who evaluated the box-counting dimension of turbulent coherent structures using 2-D PIV in the same facility. They found  $D \approx 1.5$ , which suggests a strong link between the particle cluster topology and the underlying turbulent flow. Beside the precise value of the box-counting dimension, the main observation is that large clusters of inertial particles do exhibit a scale-invariant shape in the present range of  $St_\eta$  and  $Sv_\eta$ .

In order to characterize the spatial distribution of particles within each cluster, we use the singular value decomposition (SVD) method introduced by Baker *et al.* (2017). The SVD provides the principal axes and corresponding singular values for a particle set. In two dimensions, the primary axis lies along the direction of greatest particle spread from the cluster centroid, the secondary axis being orthogonal to it (figure 12a). The corresponding singular values  $s_1$  and  $s_2$  measure the particle spread along the respective principal axes, and can be used as simple shape descriptors through the aspect ratio  $s_2/s_1$ : the limit  $s_2/s_1 = 0$  corresponds to particles arranged in a straight line, whereas  $s_2/s_1 = 1$  corresponds to a perfect circle. The PDF of the aspect ratio for all considered cases (figure 12b) shows that clusters are likely to exhibit aspect ratios between 0.4 and 0.5, reflecting a tendency to form somewhat elongated objects. Furthermore, the distribution has a positive skew, indicating that globular shapes are more common than extremely long streaks. While these observations are influenced by the 2-D nature of the technique, they are consistent with the results of Baker *et al.* (2017) who found that 3-D clusters had  $s_2/s_1$  distributions peaking around 0.5, and were positively skewed.

The orientation of the primary axis from the SVD analysis provides information on the cluster orientation in space. In figure 13(a) we plot the PDF of the cosine of  $\theta_g$ , i.e. the angle between the cluster primary axis and the vertical, evidencing a strong preference for the clusters to align with gravity. That particles tend to agglomerate along their falling direction was found in past one-way-coupled simulations (Woittiez, Jonker & Portela 2009; Dejoan & Monchaux 2013; Bec *et al.* 2014a; Ireland *et al.* 2016b; Baker *et al.* 2017), indicating the mechanism is not necessarily related to the particle backreaction on the flow. Baker *et al.* (2017) reasoned

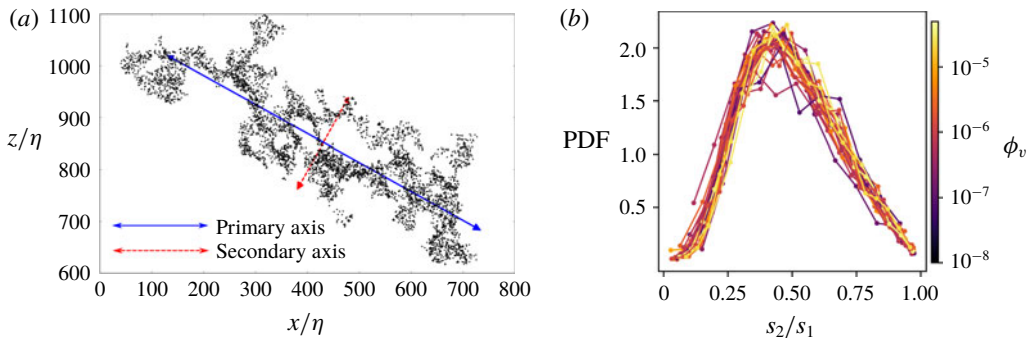


FIGURE 12. (Colour online) (a) A single coherent cluster, with primary and secondary axes as computed through SVD. The length of each arrow is proportional to the corresponding singular value. (b) PDFs of the aspect ratios of clusters for each case.

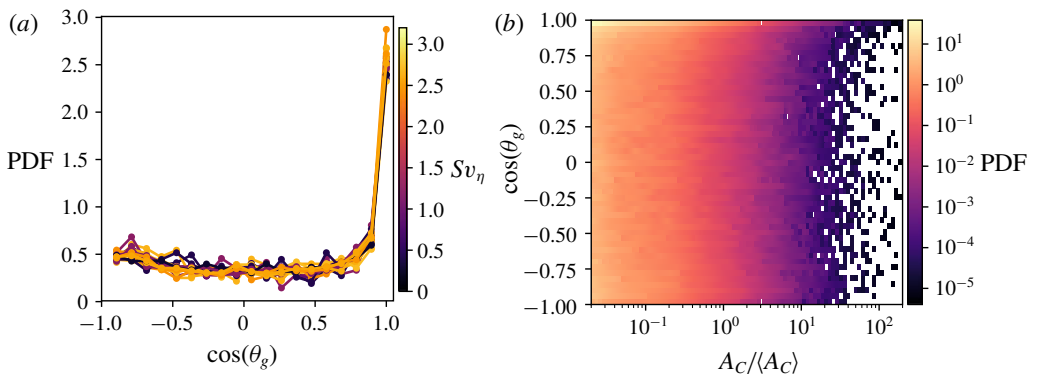


FIGURE 13. (Colour online) (a) PDFs of the cosine of the angle between clusters' primary axis and the vertical. (b) Joint PDF of angle from vertical and size of cluster.

that, especially for cases with high  $St_\eta$  and high  $Sv_\eta$ , particles are influenced by intermittent downward gusts that add to their fall speed, channelling them and creating elongated quasi-vertical structures. The joint probability distribution of  $\cos(\theta_g)$  and  $A_C$  (figure 13b) supports this view, showing that a vertical alignment corresponds to generally larger clusters. Further studies, possibly including time-resolved information, are needed to gain a mechanistic understanding of the cluster formation process.

We finally consider the concentration of particles within each coherent cluster,  $C_C = N_{PC}/A_C$ , where  $N_{PC}$  is the number of particles in each cluster. Figure 14(a,b) shows scatter plots of cluster areas and number of particles for two representative cases. The excellent fit using a power law of exponent close to unity indicates that the relationship is approximately linear, i.e. the concentration within each cluster is approximately the same for a given case. This trend is recovered for all cases. Considering the wide range of sizes, this result (reported by Baker *et al.* (2017) at a much lower  $Re_\lambda$ ) indicates again that the clusters display scale-invariant features. Figure 14(c) illustrates the average in-cluster concentration as a function of  $St_\eta$ . Despite the scatter (which points to the concurrent effects of the multiple

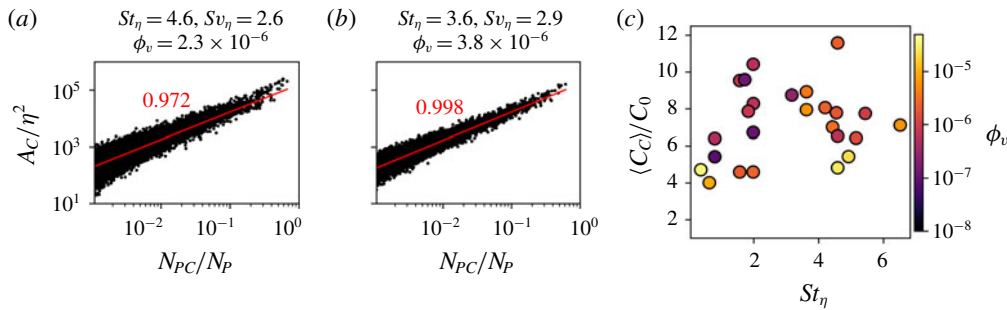


FIGURE 14. (Colour online) (a,b) Scatter plots of cluster area (normalized by the Kolmogorov scale) versus the number of particles in each cluster (normalized by the total number of particles in the domain) for two sample cases. (c) Average particle concentration in the clusters, normalized by the global concentration, plotted versus  $St_\eta$  and coloured by overall solid-volume fraction.

parameters at play), one notices an increase up to  $St_\eta \approx 2$ , followed by a plateau. The concentration within clusters can be up to an order of magnitude higher than the average over the whole particle field ( $C_0 = 1/\langle A \rangle$ ); these values are likely underestimated as particles may shadow each other at high local concentration. The present results are comparable to those from the experiments by Monchaux *et al.* (2010) and the DNS by Baker *et al.* (2017).

#### 4. Settling velocity

##### 4.1. Mean settling velocity

In this section we present and discuss the settling velocity measurements  $W_s$ , obtained ensemble averaging over all particles and realizations for each case. In figure 15(a) this is normalized by  $W_0$  (so that values greater and smaller than one indicate turbulence-enhanced and turbulence-inhibited settling, respectively) and plotted against  $St_\eta$ . The main contribution to the error is the uncertainty in  $\tau_p$  due to the particle size variance, and the non-zero vertical air velocity measured at the same time as the settling. We only plot cases in which the mean vertical fluid velocity is smaller than  $0.25W_s$ , and in fact in most cases it is  $0.01$ – $0.05W_s$ . The first observation from the plot is that the vast majority of cases display strong settling enhancement, especially for  $St_\eta \approx 1$ , which is consistent with most previous numerical (Wang & Maxey 1993; Bosse & Kleiser 2006; Dejoan & Monchaux 2013; Bec *et al.* 2014a; Ireland *et al.* 2016b; Rosa *et al.* 2016) and experimental studies (Aliseda *et al.* 2002; Yang & Shy 2003, 2005; Good *et al.* 2014). The amount of such increase is more remarkable, with the settling velocity being enhanced by a factor 2.6 for  $St_\eta \approx 1$ – $2$ . As mentioned in the Introduction, most numerical studies reported maximum increase in fall speed between approximately 10 and 90 %; some experiments (Yang & Shy 2003, 2005) found even smaller values. The present results instead indicate that turbulence can lead to a multi-fold increase in settling rate, which agrees with the conclusions from the field study of Nemes *et al.* (2017).

Similar levels of settling enhancement could also be deduced from the data of Aliseda *et al.* (2002) and Good *et al.* (2014); and while the former used concentrations where collective effects are expected ( $\phi_v \geq 10^{-5}$ ), the latter used particle loadings small enough to neglect two-way coupling ( $\phi_v \approx 10^{-6}$ ). In fact,

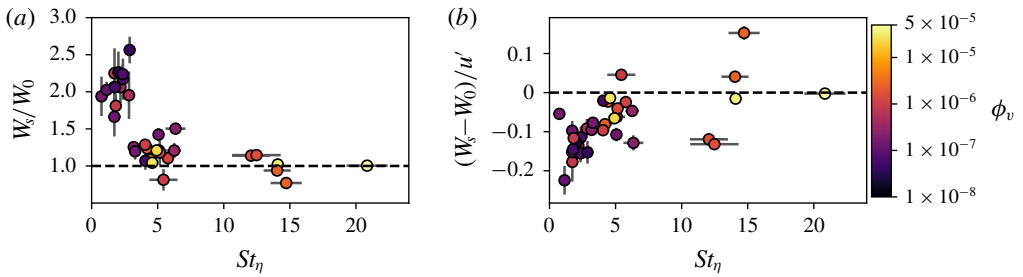


FIGURE 15. (Colour online) (a) Measured settling velocity normalized by the still-fluid Stokes value versus  $St_\eta$  and coloured by solid-volume fraction. (b) Measured settling velocity variation from the still-fluid Stokes value normalized by the fluid r.m.s. fluctuations.

those authors did not explicitly mention a multi-fold increase in vertical velocity, as they mostly plotted their data as  $(W_s - W_0)/u'$ . We present this scaling in figure 15(b), where a maximum settling enhancement of  $0.28u'$  is found for  $St_\eta \approx 1$ , again in good agreement with those authors. (Note that the vertical velocity is positive when downward, hence negative values imply settling enhancement and *vice versa*.) The scatter and the superposition of multiple factors prevent distinguishing a clear trend at the larger  $St_\eta$ . Those data points are also at relatively high  $\phi_v$ , which may have a non-trivial influence on settling, as we discuss later. Thus, the reduced settling exhibited by some of the most inertial cases, while it might appear consistent with recent results (Good *et al.* 2014; Rosa *et al.* 2016), should be considered with caution.

Figure 16 shows the results in the  $St_\eta$ – $Sv_\eta$  plane. This provides a clearer view of the data, as both parameters are expected to have significant influence on the dynamics. The maximum enhancement of settling rate occurs when both  $St_\eta$  and  $Sv_\eta$  are close to unity, in broad agreement with Good *et al.* (2014) and Rosa *et al.* (2016). The distribution of values suggests that a dependence with  $StSv$  may capture the observed trend. Figure 16(b) shows the settling enhancement ratio against the group  $St_\eta Sv_L$ , displaying a significantly improved collapse of the data. This scaling follows the argument of Nemes *et al.* (2017) that  $\tau_\eta$  and  $u'$  are the main time and velocity scales, respectively, determining increase of fall speed by turbulence. That both the small and large eddies impact the settling process has been acknowledged (Good *et al.* 2014), and already Wang & Maxey (1993) favoured  $u'$  over  $u_\eta$  as the driving parameter. Yang & Lei (1998) explicitly indicated  $\tau_\eta$  and  $u'$  as the correct flow scales, reasoning that the former controlled clustering and the latter controlled the drag experienced by the particles. The group  $St_\eta Sv_L$  can be interpreted as the ratio of the particle stopping distance ( $\tau_p^2 g$ ) and a mixed length scale ( $\tau_\eta u'$ ); settling enhancement appears most effective when this ratio is  $O(0.1)$ . This is approximately the condition at which Nemes *et al.* (2017) reported turbulence-augmented fall speeds of snowflakes in the atmospheric surface layer ( $Re_\lambda \approx 10^3$ ). Mixed-scaling arguments have been successfully used in various turbulent flows (e.g. in boundary layers, De Graff & Eaton 2000) but their theoretical underpinning poses issues which are beyond the scope of the present study.

Overall, the results presented in this section indicate that turbulence greatly enhances the settling velocity of sub-Kolmogorov particles with Stokes number around unity, which is consistent with the preferential sweeping mechanism proposed by Wang & Maxey (1993). However, a full demonstration of this view requires the

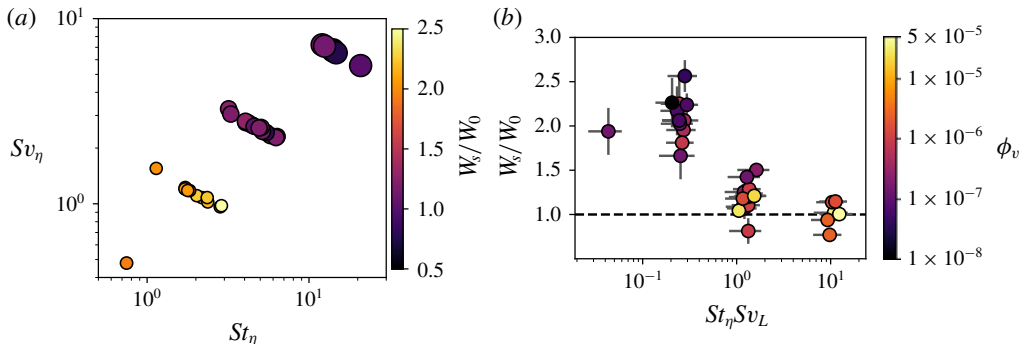


FIGURE 16. (Colour online) (a) Settling increase plotted as a function of both  $St_\eta$  and  $Sv_\eta$ . (b) Settling increase as a function of the mixed scale,  $St_\eta Sv_L$ .

simultaneous measurements of particle and fluid velocities. These will be presented in § 5.2.

#### 4.2. Settling velocity conditioned on particle concentration

To explore the interplay between the particle accumulation and settling mechanisms, we consider the fall speed associated with individual coherent clusters. In figure 17 we plot the cluster settling velocity  $W_C$ , obtained by averaging the vertical velocity of all particles belonging to a given clustered set. This is normalized by the mean settling velocity  $W_s$ , and plotted against the cluster area. Overall, clusters settle significantly faster than the mean, and there is an apparent trend of increasing fall speed with cluster size, especially for the larger objects. There are two possible interpretations for this result. On the one hand, clustered particles may affect the flow by virtue of their elevated concentration, exerting a collective drag on the surrounding fluid that results in increased settling velocity. This view reflects the argument proposed by Bosse & Kleiser (2006) in interpreting their two-way-coupled DNS study. On the other hand, particles may be merely oversampling downward regions of flow according to the preferential sweeping mechanism, and therefore cluster in such regions, leading to the observed trend. This latter interpretation, which does not require any significant two-way coupling between the dispersed and continuous phase, is consistent with the results of Baker *et al.* (2017), who reported cluster fall speeds up to twice the mean particle settling velocity in their one-way-coupled DNS.

Contrasting the effect of local and global concentration may provide further hints. In figure 18, the particle settling velocity of all particles  $W_s$  (normalized by the still-air fall speed  $W_0$ ) is plotted against the local relative concentration  $C/C_0$  (which is readily available for each particle from the Voronoï diagrams). As expected,  $W_s/W_0$  increases monotonically with  $C/C_0$ , in agreement with the trends reported by Aliseda *et al.* (2002). Indeed, particles residing in regions of low concentration are often associated with an upward velocity. We also observe, although with some scatter, the beginning of a plateau in the settling enhancement around  $C/C_0 \approx 5$ . More importantly, the plot clearly indicates that the fall speed dependence with concentration is strongly mitigated at larger global volume fractions,  $\phi_v$ . If the high fall speed of the clusters was mainly due to a collective effect of the particles on the fluid, we would expect such a speed to be further enhanced with increasing  $\phi_v$ . The fact that the opposite is

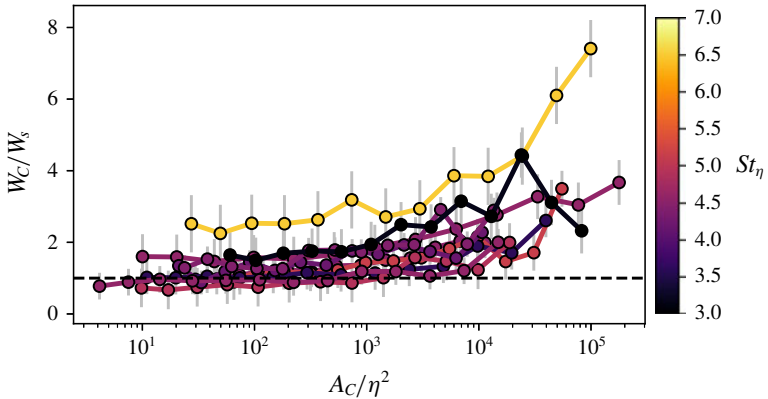


FIGURE 17. (Colour online) Average settling velocity of all clusters as a function of cluster size. Error bars indicate  $\pm$  the standard deviation.

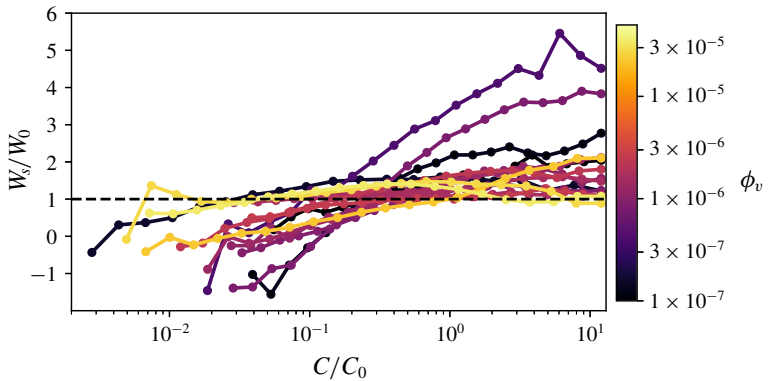


FIGURE 18. (Colour online) Normalized vertical particle velocity conditioned on the local particle concentration.

true rather suggests that the augmented cluster settling is mainly caused by preferential sweeping (or other mechanisms not depending on the mass loading). In fact, figure 18 suggests that two-way coupling may be significant over the considered range of  $\phi_v$ , but its effect may be subtle: if the particles are altering the turbulence structure, this backreaction can have a non-trivial effect on the settling rate. In general, it should be remarked that the simultaneous variation of multiple physical parameters between the considered cases (in this as in other studies) is a confounding factor in determining the role of two-way coupling, and one cannot rule out the influence of collective drag on the settling velocity (as argued by Huck *et al.* (2018)). Future dedicated studies, in which the global volume fraction is systematically varied while keeping all other parameters constant, may help shed light on this point.

## 5. Analysis of simultaneous particle and fluid fields

In this section we investigate the particle–fluid interaction by exploiting the concurrent PIV/PTV measurements of both phases. These allow us to demonstrate

and quantify effects which, although considered hallmarks of particle-laden turbulence, had rarely (if ever) been documented in experiments.

### 5.1. Preferential concentration

The fact that inertial particles oversample high-strain/low-vorticity regions, as theorized by Maxey (1987) and demonstrated numerically by Squires & Eaton (1991b), was confirmed by several later DNS studies of homogeneous turbulence, at least for  $St_\eta \leq 1$  (Chun *et al.* 2005; Bec *et al.* 2006; Cencini *et al.* 2006; Coleman & Vassilicos 2009; Salazar & Collins 2012; Esmaily-Moghadam & Mani 2016; Ireland *et al.* 2016a; Baker *et al.* 2017). To our knowledge, this prediction has not been directly verified by experiments in fully turbulent flows. Indeed, most previous laboratory studies on this topic only captured the dispersed phase (Fessler *et al.* 1994; Aliseda *et al.* 2002; Wood *et al.* 2005; Salazar *et al.* 2008; Saw *et al.* 2008; Gibert, Xu & Bodenschatz 2012), and as such could only provide results consistent with a certain picture of preferential concentration, rather than demonstrating it. We characterize the local balance of strain-rate versus rotation in the particle-laden air flow measured by PIV, using the second invariant of the velocity gradient tensor  $Q = 1/2(\boldsymbol{\Omega}^2 - \mathbf{S}^2)$ , where  $\mathbf{S}$  and  $\boldsymbol{\Omega}$  are the symmetric and anti-symmetric parts of the velocity gradient tensor (Hunt, Wray & Moin 1988). To this end, we calculate spatial derivatives using a second-order central difference scheme on the small and medium-FOV fields, where our resolution is sufficient to capture the Kolmogorov scales (Worth, Nickels & Swaminathan 2010; Hearst *et al.* 2012). From the planar data we can only determine the four components in the upper-left  $2 \times 2$  block of the full  $3 \times 3$  velocity gradient tensor. This limitation needs to be kept in mind, because 2-D sections of 3-D flows can sometimes be misleading (Perry & Chong 1994). However, several studies showed how high-resolution 2-D imaging of homogeneous turbulence yields features of the coherent structures and high-order statistics in quantitative agreement with 3-D imaging and DNS (Fiscaletti, Westerweel & Elsinga 2014; Carter & Coletti 2018; Saw *et al.* 2018). Therefore, we do not expect the qualitative results of the present analysis to be biased by the nature of the measurements.

Figure 19 shows the fraction of inertial particles found in regions where  $Q < 0$ . As expected, this fraction is larger than 50% for all cases, confirming that the particles are more likely to be found in strain-dominated regions than rotation-dominated ones. The figure also presents the percentage of clustered particles found in  $Q < 0$  regions. Interestingly, the fraction is systematically lower compared to the entire particle set. This suggests that the preferential sampling of high-strain regions might not be the main factor (or at least not the only one) for the formation of clusters over the considered parameter space. Indeed, most of our cases feature particles with  $St_\eta > 1$ , and in this regime several numerical studies indicate that the nature of the clustering mechanism is different compared to weakly inertial particles (Bec *et al.* 2007; Coleman & Vassilicos 2009; Bragg & Collins 2014; Bragg *et al.* 2015). In particular, Bragg & Collins (2014) argued for the importance of path-history effects (i.e. particles retaining memory of the velocity fluctuations they experienced), while Vassilicos and coworkers (Chen, Goto & Vassilicos 2006; Goto & Vassilicos 2008) proposed that clustering in this range is due to a sweep-stick mechanism (i.e. particles sticking to zero-acceleration points which are swept and clustered by large-scale motions). A critical discussion of these and other possible explanations is beyond the scope of this work. In fact, while instantaneous realizations and velocity statistics

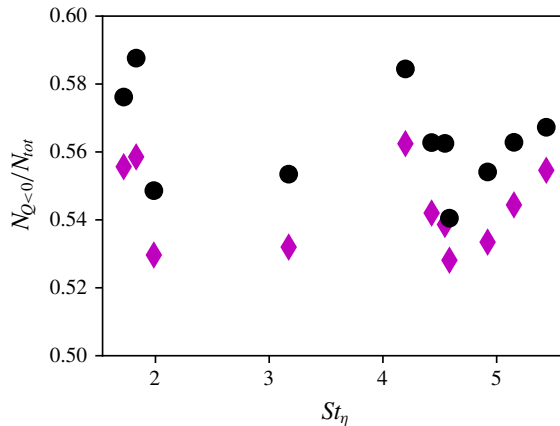


FIGURE 19. (Colour online) Fraction of particles in rotation-dominated regions. Black circles represent all particles in the field, while the purple diamonds represent only particles in coherent clusters.

may provide support to a given theory (see Obligado *et al.* 2014; Sumbekova *et al.* 2017), time-resolved measurements would be better suited to inform a mechanistic understanding of the process.

### 5.2. Preferential sweeping

As discussed in §§ 1 and 4.1, preferential sweeping is considered the most impactful mechanism by which turbulence affects the fall speed of sub-Kolmogorov particles. Its main manifestation is the tendency of particles with Stokes number of order one to oversample regions of downward velocity fluctuations. This was first theorized by Maxey & Corrsin (1986) and Maxey (1987), demonstrated numerically by Wang & Maxey (1993) and confirmed by several other analytical and computational studies (Yang & Lei 1998; Dávila & Hunt 2001; Dejoan & Monchaux 2013; Frankel *et al.* 2016; Baker *et al.* 2017). While laboratory studies (Aliseda *et al.* 2002; Yang & Shy 2003, 2005; Good *et al.* 2014) and field observations (Nemes *et al.* 2017) showed results consistent with this picture, no direct experimental verification has been reported. Similar to preferential concentration, the challenges associated with two-phase measurements may be responsible.

We provide such verification first by considering the particle concentration conditionally averaged on the local fluid velocity. This is obtained by counting the number of inertial particles in each PIV interrogation window, and binning the results by the value of  $W_f/W_0$  (because the mean vertical fluid velocity is negligibly small, total and fluctuating components coincide). The relative concentration is calculated as the number of particles in each bin, divided by the sum of window areas associated with that bin and finally normalized by the global concentration. The procedure is equivalent to that originally adopted by Wang & Maxey (1993) and later by Baker *et al.* (2017) to analyse DNS results, with the PIV interrogation windows in lieu of the computational cells. In figure 20 we show the result for a representative case, clearly indicating downward fluid velocity corresponding to higher local concentration. When the process is repeated only considering particles belonging to clusters, the trend is significantly more pronounced. This is consistent with the result that clusters

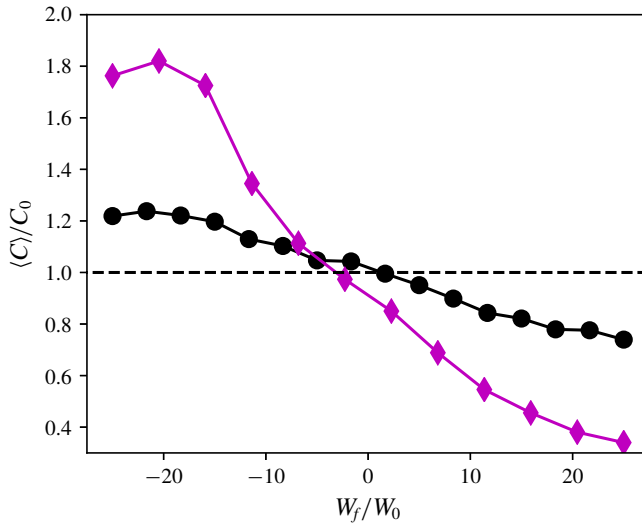


FIGURE 20. (Colour online) Example case of the relative particle concentration conditioned on the vertical fluid velocity (normalized by the still-air settling velocity.) Black circles indicate the full particle set, while purple diamonds represent only particles in clusters.

fall at faster speeds than the rest of the particles (figure 17). At the same time, it also supports the idea that preferential sweeping plays an important role in the clustering of settling particles.

To quantify the impact on the settling rate, we consider the vertical component of the fluid velocity at the particle location,  $W_f(\mathbf{x}_p)$  (figure 21). The latter is approximated via a piecewise linear interpolant between the particle position and the four closest fluid velocity vectors; tests with other schemes indicate only a weak dependence with the interpolation method. Error analysis based on the fluid velocity gradient statistics (see Carter *et al.* 2016; Carter & Coletti 2017) yields uncertainty on  $W_f(\mathbf{x}_p)$  around 2–7%  $u'$ . Despite some scatter partly attributable to the several factors at play, the results indicate that preferential sweeping is important for most considered regimes, being the strongest for  $St_\eta = O(1)$ .

Comparing figures 15(b) and 21, the oversampling of downward fluid velocity regions seems to account for a large part of the settling enhancement. A more quantitative account can be given in the framework of the point-particle approximation. Retaining only drag and gravity in the particle equation of motion, the fall speed can be approximated as (Wang & Maxey 1993):

$$\langle W_s \rangle \approx \langle \mathbf{u}_f(\mathbf{x}_p, t) \rangle + \frac{\tau_p g}{\langle f \rangle}, \quad (5.1)$$

where  $\mathbf{u}_f(\mathbf{x}_p)$  is the fluid velocity vector at the particle location obtained via the piecewise-linear interpolation, and  $\langle f \rangle$  is the ensemble average of the Schiller & Naumann correction factor in (2.1),  $f = 1 + 0.15Re_p^{0.687}$ . We can directly verify this approximation using the instantaneous  $Re_p$  measured from the simultaneous PIV/PTV measurements (which will be discussed further in the next section). Figure 22 shows the ratio between the fall speed calculated from (5.1) and the measured values. This

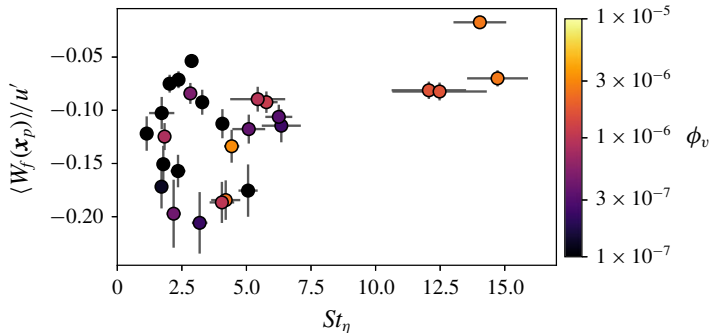


FIGURE 21. (Colour online) Vertical fluid velocity at particle location, normalized by the fluid r.m.s. velocity, plotted versus particle Stokes number.

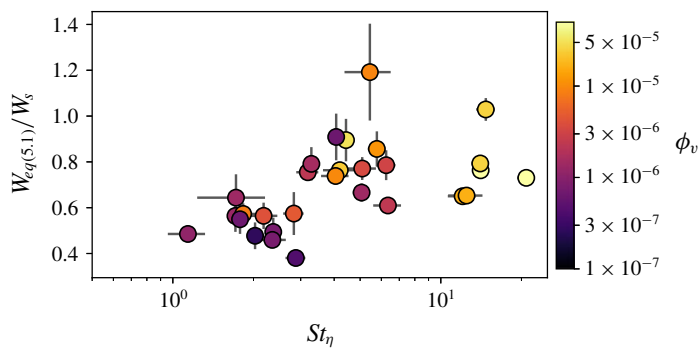


FIGURE 22. (Colour online) Prediction of settling velocity based on (5.1) normalized by the measured settling velocities, versus particle Stokes number.

formulation consistently underpredicts the measured fall speed. Such a discrepancy between experiments and theory suggests that the one-way-coupled point-particle approach, while providing the correct qualitative trend, is missing significant aspects of the particle–fluid interaction. We investigate possible sources of the mismatch in § 5.4, where we consider the instantaneous slip velocity.

### 5.3. Crossing trajectory and continuity effects

Since Yudine (1959), it has been recognized that the drift induced by body forces such as gravity causes heavy particles to decorrelate from their past velocity faster than a fluid element. This so-called crossing trajectory effect can be quantified by the Lagrangian autocorrelation of the particle velocity (Elghobashi & Truesdell 1992). For large drift velocities, this reduces to the fluid space–time correlation in an Eulerian frame (Csanady 1963; Squires & Eaton 1991a). In this limit, as the longitudinal integral scale is twice the transverse one, the particle dispersion parallel to the drift direction is double the dispersion perpendicular to it (the so-called continuity effect; Csanady 1963; Wang & Stock 1993). The footprints of these effects are visible in the Eulerian particle velocities. In figure 23 we present a scatter plot of the vertical and horizontal r.m.s. particle velocity fluctuations ( $W_{p,rms}$  and  $U_{p,rms}$ , respectively), normalized by the r.m.s. fluid fluctuations in the respective directions ( $u'_z$  and  $u'_x$ ) to

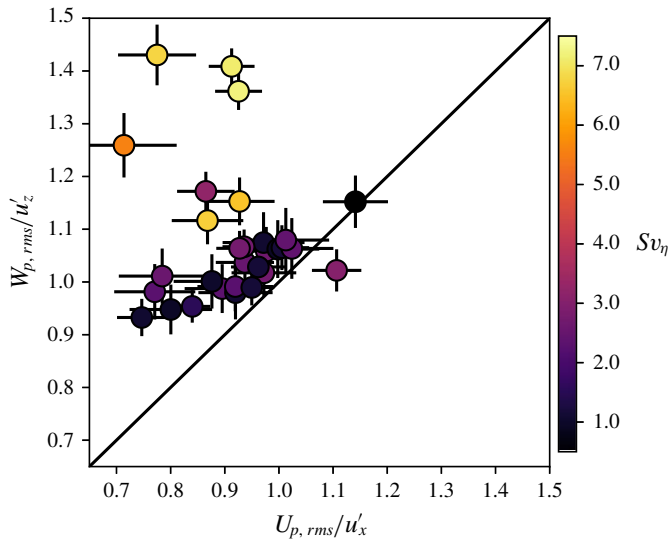


FIGURE 23. (Colour online) Ratio of vertical particle to fluid r.m.s. velocity versus ratio of the same horizontal velocities.

account for the anisotropy in our facility. The normalized vertical fluctuations of the particles exceed those in the horizontal direction, the disparity being more substantial for larger  $Sv_\eta$ . This trend is consistent with the continuity effect, and in line with previous analysis by Wang & Stock (1993) and measurements by Good *et al.* (2014): the falling particles have more time to respond to the vertical fluid fluctuations, due to the larger longitudinal integral scale compared to the transverse one.

#### 5.4. Particle–fluid relative velocity

The relative (slip) velocity between suspended particles and the surrounding fluid plays a vital role in both the particle kinematics and the interphase coupling. The slip velocity determines the exchanged forces and the local flow regime around a particle (Maxey & Riley 1983; Calzavarini *et al.* 2008; Bellani *et al.* 2012), and is critical for the momentum two-way coupling with the fluid (Sahu *et al.* 2016). It is also a key quantity for modelling sub-grid-scale dynamics in large-eddy simulations of particle-laden turbulence (Soldati & Marchioli 2009). Due to the abovementioned difficulties in measuring both phases, the slip velocity has been reported by only a few experimental studies, notably Kiger & Pan (2002) and Khalitov & Longmire (2003) in wall-bounded turbulent flows, and Yang & Shy (2005) and Sahu *et al.* (2016) in homogeneous turbulence.

Here we evaluate the slip velocity as  $\mathbf{u}_{\text{slip}} = \mathbf{v}_p - \mathbf{u}_f(\mathbf{x}_p)$ , where  $\mathbf{v}_p$  is the particle velocity vector. In the present measurements we only have access to the in-plane projection of those vectors. Here we only use data from the small and intermediate FOVs. We remark that the relevant definition of slip velocity (as it appears, e.g. in Stokes drag law) is the difference between the particle velocity and the undisturbed fluid velocity evaluated at the particle location. Because in the considered cases  $d_p < \eta$  and  $Re_{p,0} \leq 1$ , the region of perturbation from an individual particle (as estimated, e.g. by the Oseen solution) is expected to be a few particle diameters, i.e. typically smaller than the Kolmogorov scale. Under this assumption, the interpolated

fluid velocity approximates the undisturbed velocity. However, as we shall see, the instantaneous particle Reynolds number  $Re_p$  can reach much larger values than  $Re_{p,0}$ .

Figure 24(a) presents PDFs of the slip velocity magnitude normalized by the fluid r.m.s. fluctuation. At the higher  $St_\eta$ ,  $\mathbf{u}_{\text{slip}}$  can significantly exceed  $u'$ , suggesting that the potential energy transferred to the fluid by the fast falling particles is considerable with respect to the turbulent kinetic energy. We will return to this point in § 5.5. In figure 24(b) we plot the PDF of the vertical component of the slip velocity  $W_{\text{slip}}$ , normalized by the still-air particle settling velocity  $W_0$ . The mean vertical slip is approximately equal to  $W_0$ , as one expects from (5.1). However, the standard deviation is large and, especially for the lower  $St_\eta$ , greatly exceeds the mean value; indeed, the probability of an upward particle slip is significant. This behaviour is consistent with the simulations of particle-laden wall-bounded turbulence by Zhao, Marchioli & Andersson (2012), who found that the r.m.s. fluctuations of both streamwise and wall-normal slip velocities were several times greater than their mean. The r.m.s. slip velocities are presented in figure 24(c,d) separating horizontal and vertical components and normalizing by the r.m.s. fluid velocity fluctuations in their respective directions. The slip velocity fluctuations increase with  $St$ , also consistent with the results of Zhao *et al.* (2012): the heavier particles increasingly move independently from the fluid, and their r.m.s. slip velocities reach levels comparable to the r.m.s. fluid fluctuations. The vertical r.m.s. is consistently higher than the horizontal. This is likely a consequence of the vertical r.m.s. velocity of the particles being larger than the horizontal one, as discussed in the previous section.

The magnitude of the in-plane slip velocity can be used to calculate the instantaneous particle Reynolds number. The PDFs of  $Re_p$  for various cases are plotted in figure 25(a), with the vertical lines indicating the respective theoretical  $Re_{p,0}$ . The large slip variance results in long tails of the distributions: while the wake-shedding regime is never achieved, there is a sizeable probability of  $Re_p$  being an order of magnitude larger or smaller than the nominal value. The values are in fact somewhat underestimated, because the out-of-plane slip is not accounted for.

The slip velocity and Reynolds number can be used to evaluate the drag coefficient on the settling particles. In the presence of background turbulence, this is expected to differ from the standard drag in a steady uniform flow (Bagchi & Balachandar 2003). The latter can be estimated following the Schiller & Naumann correction for finite Reynolds number:

$$C_{d,SN} = \frac{24}{Re_{p,0}} (1 + 0.15 Re_{p,0}^{0.687}). \quad (5.2)$$

As suggested by Balachandar & Eaton (2010), for particles settling in zero-mean-flow homogeneous turbulence, one can evaluate an effective drag coefficient:

$$C_{d,\text{eff}} = \frac{24}{\langle Re_v \rangle \langle W_p \rangle} \left| \langle \mathbf{u}_{\text{slip}} \rangle + 0.15 \left( \frac{d_p}{v} \right)^{0.687} \langle \mathbf{u}^{1.687} \rangle \right|, \quad (5.3)$$

where  $Re_v = d_p |\mathbf{v}_p| / v$ . This may differ from the  $C_{d,SN}$  owing to three main factors: the mean fluid velocity seen by the particles being non-zero (e.g. due to preferential sweeping); the nonlinear relation between drag and slip velocity; and possible two-way coupling. Most previous studies concerned with the influence of ambient turbulence on  $C_d$  considered larger  $Re_p$  compared to the present case (typically of order  $10^2$ – $10^3$ ; e.g. Wu & Faeth 1994; Warnica, Renksizbulut & Strong 1995; Bagchi & Balachandar 2003). In these cases, the effect on the mean drag was found to

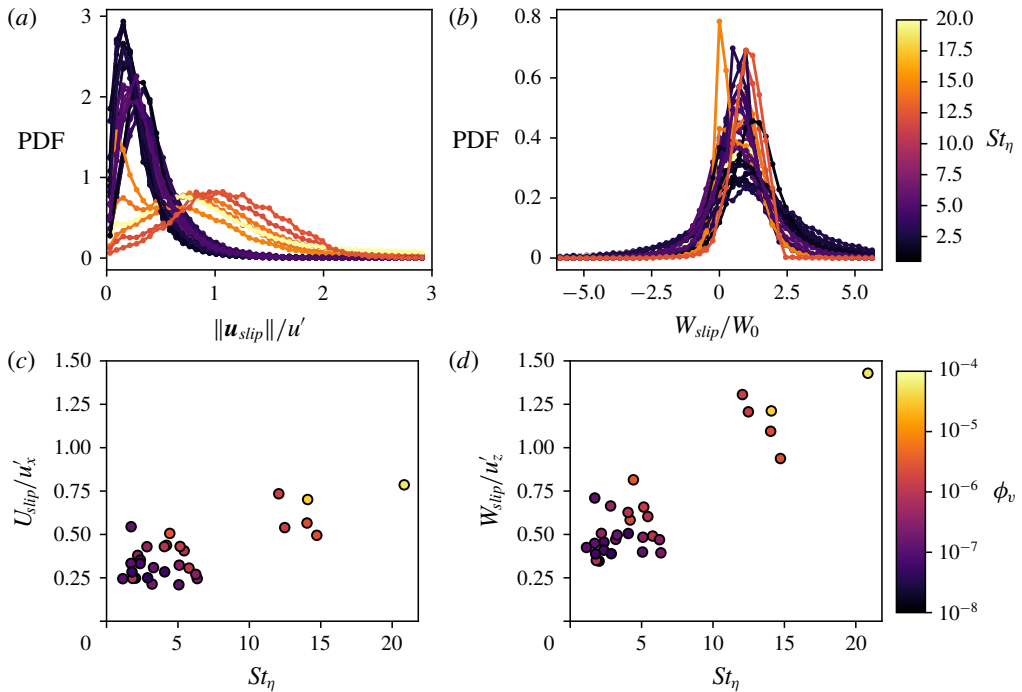


FIGURE 24. (Colour online) Probability density functions of slip velocity magnitude normalized by fluid r.m.s. velocity (a), and vertical slip velocity (b) normalized by the still-fluid settling. (c,d) Plots of horizontal and vertical r.m.s. particle slip velocity, respectively, normalized by the fluid r.m.s. fluctuations along the corresponding direction.

be small. Bagchi & Balachandar (2003), however, recognized the potential importance of preferential flow sampling for particles falling freely through turbulence. Here we use (5.2) and (5.3) and plot the ratio  $C_{d,\text{eff}}/C_{d,\text{SN}}$  in figure 25(b). There is a significant reduction in effective drag over the  $St_\eta$  range displaying preferential sweeping. This is consistent with the early measurements of Rudoff & Bachalo (1988), who found substantially reduced drag for liquid droplets in turbulent air. We also observe a clear increasing trend with  $St_\eta$ . This is likely a consequence of diminishing preferential sweeping effects, giving way to those of nonlinear drag and possibly loitering (Good *et al.* 2014). We remark, however, that the high- $St$  data points are affected by larger uncertainty due to two factors: non-negligible perturbation of the local fluid velocity by the particles (because of their relatively large  $Re_p$ ), and limited spatial resolution (because those are imaged with the intermediate FOV). Thus, further analysis and measurements are warranted for those regimes.

We then consider the spatial orientation of the particle slip velocity. Figure 26(a) shows the PDF of  $\cos(\theta)$ ,  $\theta$  being the angle between  $\mathbf{v}_p$  and  $\mathbf{u}_f(x_p)$ . For moderate particle inertia ( $St_\eta < 10$ ) the fluid and particle velocity vectors tend to be closely aligned, with  $\theta < 30^\circ$  in more than 90 % of the instances. As expected, the more inertial particles are more likely to display a velocity orientation substantially different from the fluid velocity. The probability of oppositely aligned vectors is also non-negligible, possibly due to weak upward gusts that are unable to reverse the particle settling motion. The probability distribution of slip orientation and magnitude is illustrated by the wind rose diagrams in figure 26(b) for selected cases. The length

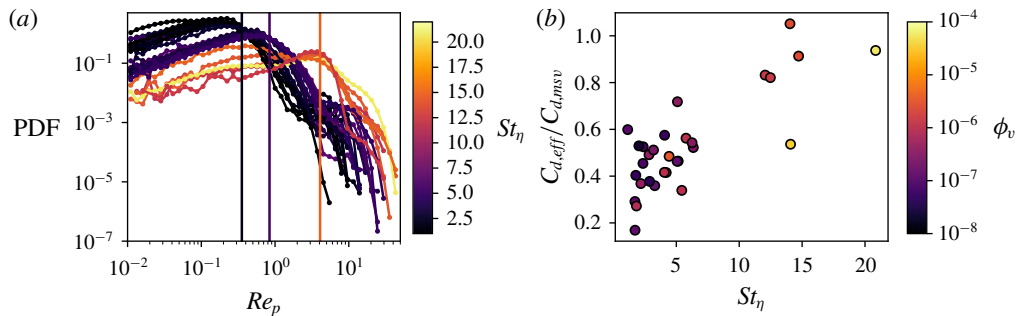


FIGURE 25. (Colour online) PDFs of instantaneous particle Reynolds number. Vertical lines represent average Reynolds particle number based on the Stokes still-fluid settling velocity for each respective grouping of experiments. Panel (b) shows the ratios between drag coefficients (5.2) and (5.3), showing reduced drag when the ‘effective drag’ model is used.

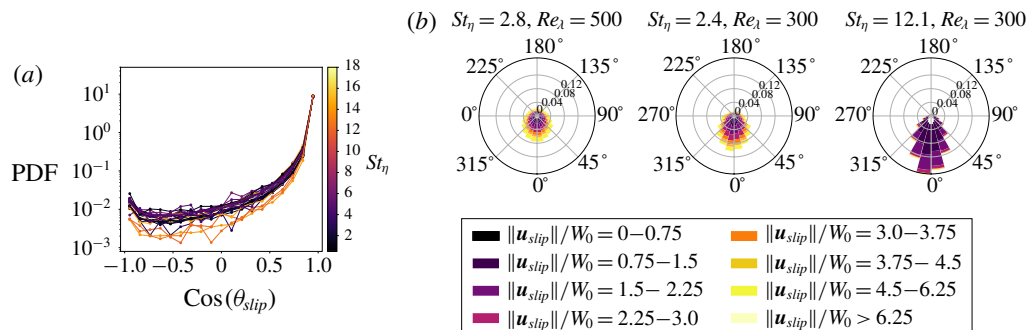


FIGURE 26. (Colour online) PDF of the cosine of the angle between the particle velocity and the fluid velocity at the particle location (a). (b) Three example cases showing the probability distribution of the slip velocity orientation and magnitude.

of each spoke represents the probability associated with its orientation; additionally, each spoke is broken down into segments representing the probability of a certain slip velocity magnitude (normalized by  $W_0$ ). In all cases the slip velocity favours the downward direction, as expected. In the larger  $Re_\lambda$  cases, however, the strong fluid velocity fluctuations mitigate this tendency and the azimuthal distribution of the particle slip is less skewed. As discussed above, particles with  $St_\eta \approx 1$  can have slip velocities several times larger than their still-air fall speed. On the other hand,  $\mathbf{u}_{slip}$  for the more inertial cases is closer in magnitude to  $W_0$  and mostly oriented downward (typically within  $\pm 45^\circ$  from the vertical), confirming that these particles follow more ballistic downward trajectories.

### 5.5. Turbulence modification by particles

We finally consider the scale-by-scale effect of the particles on the fluid turbulent fluctuations. We consider the second-order structure functions, which contain analogous information as the energy spectra used in most previous studies:

$$D_{ii}(\mathbf{r}) = \overline{[u_i(\mathbf{x} + \mathbf{r}) - u_i(\mathbf{x})]^2}. \quad (5.4)$$

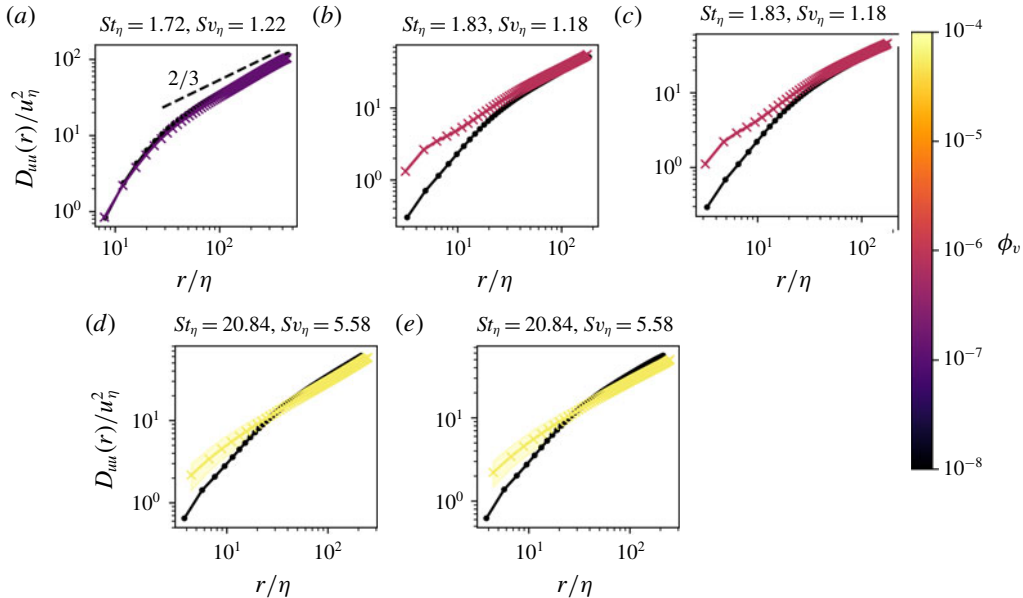


FIGURE 27. (Colour online) Horizontal (*a,b,d*) and vertical (*c,e*) longitudinal structure functions for laden (colour coded by volume fraction) and unladen (black) multiphase flows. The shaded regions represent 95 % bootstrap confidence bounds.

Here  $\mathbf{x}$  is the generic location on the imaging plane,  $\mathbf{r}$  is the separation vector and  $u_i$  is the  $i$ th component of the velocity fluctuations. Thus, we denote as  $D_{uu}$  and  $D_{ww}$  the structure functions associated with the horizontal and vertical components. We focus on longitudinal structure functions (i.e. with separations parallel to the velocity components), the transverse structure functions yielding similar results. For this analysis we use only small and intermediate FOVs, in order to resolve a sufficient fraction of the fine-scale fluctuations.

Figure 27 displays horizontal and vertical structure functions for representative cases, comparing the laden and unladen measurements. At very low volume fractions ( $\phi_v = O(10^{-7})$ ), the particles marginally affect the energy distribution across scales, and the expected scaling  $D_{ii}(r) \sim r^{2/3}$  is approached entering the inertial range according to Kolmogorov theory (figure 27*a*). At significant loadings ( $\phi_v = O(10^{-5})$ ), we observe an increase of turbulent energy at small scales. For  $St_\eta = O(1)$  (figure 27*b*) the laden and unladen curves approach each other at larger scales, possibly leading to a cross-over which however is not captured within the FOV. At  $St_\eta = O(10)$ , the cross-over happens at smaller scales as demonstrated in figure 27(*d*), in which particles appear to excite turbulent fluctuations at the small scales and modulate them at the large scales. This behaviour (sometimes termed pivoting) was reported by several numerical studies, as reviewed in detail by Poelma & Ooms (2006). Most of those (e.g. Sundaram & Collins 1999; Ferrante & Elghobashi 2003) showed the cross-over wavenumber to increase with increasing particle response time, consistent with our observations. The only previous experimental study to clearly demonstrate the pivoting effect was, to our best knowledge, the one from Poelma *et al.* (2007). However, a direct comparison is difficult as these authors considered spatially decaying turbulence at maximum  $Re_\lambda \approx 29$ .

The vertical velocity structure functions (figure 27c,e) display the same behaviour as their horizontal counterpart (figure 27b,d), suggesting that the turbulence responds to the presence of the particles in similar ways in both directions. It is indeed verified that the anisotropy ratio  $u'_x/u'_z$  is not significantly affected by the particles. Poelma *et al.* (2007) and Frankel *et al.* (2016) found that particles enhanced the fluid velocity fluctuations aligned with gravity compared to the transverse ones, whereas in Hwang & Eaton (2006b) the level of isotropy was marginally influenced even at particle mass loadings that heavily modulated the turbulence intensity. Among these studies, Hwang & Eaton considered a much higher Reynolds number ( $Re_\lambda \approx 240$ ), comparable to the present study. One may conjecture that the wide range of scales allows for a redistribution of the energy among the different components; certainly, further studies that systematically investigate the role of  $Re_\lambda$  are needed.

Even for the higher volume fractions, the changes in the fluid turbulence intensities in both vertical and horizontal directions (not presented) are scattered within the measurement uncertainty, with no consistent trend in terms of  $St_\eta$ ,  $Sv_\eta$  or  $\phi_v$ . This suggests that the turbulence augmentation/attenuation, over different scales and from different mechanisms, largely compensate each other, at least in the considered range of parameters. On one hand, particles increase the overall inertia of the mixture and locally enhance the dissipation around them, modulating the turbulence; on the other hand, the drag force exerted by the falling particles perturbs the fluid and excites the turbulence (Balachandar & Eaton 2010). Both effects are amplified for larger and heavier particles (which provide higher loading, distort more the flow around them and shed more energetic wakes). For comparison, Hwang & Eaton (2006a) investigated particles with  $St_\eta \approx 50$  settling in homogeneous turbulence and measured a reduction of r.m.s. fluid velocity of approximately 10–15 % for a mass fraction of 0.1 (close to the highest loading considered in the present measurements). The balance between opposing effects was demonstrated by measurements obtained in the same facility in micro-gravity (Hwang & Eaton 2006b), where the turbulence modulation was found to be greater than in the fixed laboratory frame. Hwang & Eaton (2006b) also compared their laboratory results against DNS studies which showed significantly smaller turbulence attenuation. While this suggested that the point-particle approach used in the simulations missed important physics, the DNS were also at significantly smaller  $St_\eta$ , between 1 and 11 and comparable to the present cases.

## 6. Discussion and conclusions

The present experimental approach has allowed us to gain insight into several outstanding issues in particle-laden turbulence. The jet-stirred homogeneous air turbulence chamber is particularly suitable to characterize the considered regime: the lack of mean flow enables the unbiased measurement of the settling velocity, also yielding a much larger dynamic range for the velocity fluctuations compared to wind tunnel experiments (Carter & Coletti 2017). Moreover, the large region of homogeneous turbulence is crucial for the particles to interact with the full range of turbulent scales (Bellani & Variano 2014). The simultaneous imaging of both phases allows the characterization of their interplay, within the inherent limits posed by the imaging accuracy and its planar nature. Finally, the relatively high  $Re_\lambda$  warrants the separation of scales needed to identify the dominant flow parameters.

We have characterized the particle spatial distribution using both RDF and Voronoï diagrams. The former show a power-law decay over (and beyond) the near-dissipative scales, followed by a long exponential tail. The latter indicates that clustering

extends far beyond the dissipation range, although the particle field does not display scale-invariant properties over such distances. It is confirmed that clustering is most intense for  $St_\eta \approx 1$ , but remains significant even for more inertial particles, which in fact cluster over larger regions. This is due partly to their response time being comparable to the time scales of larger eddies, and partly to the effect of gravity. It was indeed reported in several numerical investigations that gravitational settling enhances clustering for  $St_\eta > 1$  (see Ireland *et al.* 2016b). Gravity is unavoidable in laboratory experiments, thus its effect is hard to discern from inertia. However, our results for various  $St_\eta$  and  $Sv_\eta$  are at least consistent with this trend. We argue that such an effect is associated with  $u'$  becoming the relevant velocity scale for the interaction of turbulence with fast-falling particles: the latter quickly decorrelate from Kolmogorov-size eddies, and rather respond to large-scale velocity fluctuations. Indeed, the fraction of clustered particles and the cluster size generally increases with particle inertia.

The Voronoï diagram method generally confirms the findings from the RDF analysis, and allows us to explore further aspects of the particle distribution, focusing on individual clusters. The properties of those discrete groups of highly concentrated particles bears particular significance, as these may interact with one other and, by virtue of their collective action, modify the surrounding flow (Monchaux *et al.* 2012). We find that sufficiently large clusters (i.e. coherent clusters in the definition of Baker *et al.* (2017) follow power-law size distributions over several decades, and display a precise fractal dimension. Therefore, borrowing the terminology proposed by Paola, Kim & Mastorakos (2009) to describe scale invariance in geomorphology, these objects exhibit both internal similarity (between the system and small parts of it) and external similarity (between the system and small copies of it). This also suggests that they follow (without necessarily replicating) the self-similar topology of the underlying turbulence. The clusters are usually elongated and often aligned with the vertical direction. The mean particle concentration in a cluster can be an order of magnitude higher than the average, and is largely independent on the cluster size.

It may appear surprising that particle clusters display both internal and external similarity, and over such a wide range of scales. After all, turbulence is known to display strong departures from self-similarity associated with its intermittent behaviour. However, a few considerations are in order. First, intermittency is most evident in high-order quantities in which the size and shape of the clusters of inertial particles might be relatively insensitive. In fact, the intense vortex filaments usually regarded as responsible for scale-variant behaviours are precisely the structures where particles of  $St_\eta = O(1)$  are unlikely to be found. Also, by focusing on coherent clusters, we set a size threshold larger than the scale over which intermittency is manifest. One point that deserves deeper investigation is that, unlike the Voronoï-based cluster topology, two-point measures of clustering such as RDFs do not display scale invariance in the inertial range (as also confirmed by our experiments). Bragg *et al.* (2015) analysed the scaling of RDFs in this range, and their arguments may also be the basis of a theoretical investigation of the inertial-scale cluster dynamics; this however is outside the scope of the present work.

One of the major findings of the study is that, for  $St_\eta$  and  $Sv_\eta$  of order unity and in the considered range of  $Re_\lambda$ , turbulence produces almost a threefold increase in settling velocity with respect to quiescent conditions. Such a dramatic effect has far-reaching consequences in a myriad of natural and engineering settings, from atmospheric precipitation to industrial processes and pollutant dispersion. Remarkably, the effects of turbulence on the fall speed of hydrometeors have only recently begun

to be addressed in field studies (Garrett & Yuter 2014). In particular, the present results are consistent with the measurements by Nemes *et al.* (2017) who imaged snowflakes settling in the atmospheric surface layer. The data are best collapsed by a mixed scaling based on  $\tau_\eta$  and  $u'$ , which may reflect how the latter is indeed the relevant velocity scale ruling the settling enhancement. This argument is consistent with the idea of distant-scale interaction, which has been used in wall-bounded flows to explain the success of mixed scaling of the streamwise turbulent fluctuations (Marusic & Kunkel 2003).

Clusters fall even faster than the average particle in turbulence. In the considered range of parameters, this appears to be due to the particle tendency to oversample downward flow regions, according to the preferential sweeping mechanism. The latter is shown to be responsible for the observed enhanced settling, and in the present regime is a more recognizable feature than the preferential concentration in high-strain/low-vorticity regions. Owing to the crossing trajectory and continuity effects, the vertical velocity fluctuations of the particles are stronger than the horizontal ones. The r.m.s. of the vertical slip velocities are also larger than the horizontal, and both can largely exceed their respective mean values. Thus, the actual particle Reynolds number can greatly differ from the nominal value usually used to correct Stokes law. Indeed, the effective drag coefficient calculated via the simultaneous two-phase measurements is found to depart significantly from the standard estimate. This points to clear limitations of the point-particle approach, perhaps accounting for some of the quantitative disagreement between experiments and DNS at matching conditions (Good *et al.* 2014).

At sufficient concentrations, the particles excite small-scale fluid velocity fluctuations, which however may represent a small fraction of the turbulent kinetic energy. For the heavier particles, we generally observe a reduction of turbulent energy at the larger scales. Over the considered range of parameters, the measurements did not indicate a trend of augmentation versus attenuation of the overall turbulence intensity. This is perhaps not surprising, considering the multiple counteracting effects contributing to turbulence modification at the different scales, along with the difficulty of varying one parameter at a time. Dedicated experiments in which the volume fraction is systematically varied over a wide range, keeping all other settings constant, stand a higher chance of providing some conclusive answer. This was not the main goal of the present work, and it will be the focus of a future campaign. Such a study, however, is expected to be challenging: for sub-Kolmogorov particles and relatively high  $Re_\lambda$ , substantial mass loadings require large number densities, posing problems for the fluid velocimetry. Those can be alleviated by imaging at very high resolution; but this limits the FOV, and consequently the insight into multi-scale mechanisms. Therefore, the use of very large sensors and/or the simultaneous deployment of multiple cameras appear necessary to fully quantify two-way coupling effects in preferentially concentrated particle-laden turbulence.

Overcoming the limitations of planar measurements will require a leap in performance of 3-D particle imaging at high concentrations. Novel approaches based on tomographic PTV are breaking grounds in single-phase velocimetry (Schanz, Gesemann & Schröder 2016), and may be applied to inertial particles. Advanced numerical methods are also expected to shed new light: particle-resolved DNS has been successfully applied to investigate relatively large particles (Lucci *et al.* 2010; Naso & Prosperetti 2010; Cisse, Homann & Bec 2013; Gao, Li & Wang 2013; Tenneti & Subramaniam 2014; Uhlmann & Doychev 2014; Fornari, Picano & Brandt 2016), and recently even Kolmogorov-sized particles (Schneiders, Meinke & Schröder

2017). The ever-increasing computational power will soon allow resolving even smaller objects, elucidating the role of mechanisms such as the local hydrodynamic interaction between particles (Wang *et al.* 2007). Still, capturing truly collective effects with this approach will require enormous computational resources. Considering the present case as an example (e.g.  $L \approx 100$  mm and  $d_p \approx 50$   $\mu\text{m}$ ), a cubic domain of size  $2\pi L$  with a volume fraction of  $5 \times 10^{-5}$  contains  $O(10^8)$  particles. Low-order methods able to incorporate the essential physics are therefore sorely needed; the role of experiments and particle-resolved simulations in informing and validating them will be essential.

### Acknowledgements

The present work was supported in part by the US Army Research Office (Division of Earth Materials and Processes, grant W911NF-17-1-0366). A.J.P. is supported by a National Science Foundation Graduate Research Fellowship. L.B. is supported by a National Defense Science and Engineering Graduate Fellowship. The manuscript benefited from the insightful comments of the anonymous referees. We are thankful to D. Carter and O. Amili for valuable help during the measurement campaign, and many fruitful discussions. Alec would especially like to thank A. Nemes for all his guidance and help on the software side of things. Lastly, a small thanks to J. Herzfeld and G. Petersen, both of whom helped run an experiment or two when they were supposed to be having fun visiting Alec.

### REFERENCES

- ALISEDA, A., CARTELLIER, A., HAINUX, F. & LASHERAS, J. C. 2002 Effect of preferential concentration on the settling velocity of heavy particles in homogeneous isotropic turbulence. *J. Fluid Mech.* **468**, 77–105.
- AYYALASOMAYAJULA, S., GYLASON, A., COLLINS, L. R., BODENSCHATZ, E. & WARHAFT, Z. 2006 Lagrangian measurements of inertial particle accelerations in grid generated wind tunnel turbulence. *Phys. Rev. Lett.* **97** (14), 144507.
- BAGCHI, P. & BALACHANDAR, S. 2003 Effect of turbulence on the drag and lift of a particle. *Phys. Fluids* **15** (11), 3496–3513.
- BAKER, L., FRANKEL, A., MANI, A. & COLETTI, F. 2017 Coherent clusters of inertial particles in homogeneous turbulence. *J. Fluid Mech.* **833**, 364–398.
- BALACHANDAR, S. 2009 A scaling analysis for point particle approaches to turbulent multiphase flows. *Intl J. Multiphase Flow* **35** (9), 801–810.
- BALACHANDAR, S. & EATON, J. K. 2010 Turbulent dispersed multiphase flow. *Annu. Rev. Fluid Mech.* **42** (1), 111–133.
- BATESON, C. P. & ALISEDA, A. 2012 Wind tunnel measurements of the preferential concentration of inertial droplets in homogeneous isotropic turbulence. *Exp. Fluids* **52** (6), 1373–1387.
- BEC, J. 2003 Fractal clustering of inertial particles in random flows. *Phys. Fluids* **15**, L81.
- BEC, J., BIFERALE, L., BOFFETTA, G., CELANI, A., LANOTTE, A., MUSACCIO, S. & TOSCHI, F. 2006 Acceleration statistics of heavy particles in turbulence. *J. Fluid Mech.* **550**, 349–358.
- BEC, J., BIFERALE, L., CENCINI, M. & LANOTTE, A. S. 2010 Intermittency in the velocity distribution of heavy particles in turbulence. *J. Fluid Mech.* **646**, 527–536.
- BEC, J., BIFERALE, L., CENCINI, M., LANOTTE, A., MASUCCHIO, S. & TOSCHI, F. 2007 Heavy particle concentration in turbulence at dissipative and inertial scales. *Phys. Rev. Lett.* **98**, 084502.
- BEC, J., CENCINI, M., HILLERBRAND, R. & TURITSYN, K. 2008 Stochastic suspensions of heavy particles. *Physica D* **237**, 2037–2050.

- BEC, J., HOMANN, H. & RAY, S. S. 2014a Gravity-driven enhancement of heavy particle clustering in turbulent flow. *Phys. Rev. Lett.* **112** (18), 184501.
- BEC, J., HOMANN, H. & RAY, S. S. 2014b Gravity-driven enhancement of heavy particle clustering in turbulent flow. *Phys. Rev. Lett.* **112**, 184501.
- BELLANI, G., BYRON, M. L., COLLIGNON, A. G., MEYER, C. R. & VARIANO, E. A. 2012 Shape effects on turbulent modulation by large nearly neutrally buoyant particles. *J. Fluid Mech.* **712**, 41–60.
- BELLANI, G. & VARIANO, E. A. 2014 Homogeneity and isotropy in a laboratory turbulent flow. *Exp. Fluids* **55** (1), 1646.
- BENDAT, J. S. & PIERSOL, A. G. 2011 *Random Data Analysis and Measurement Procedures*. Wiley.
- BEWLEY, G. P., SAW, E.-W. & BODENSCHATZ, E. 2013 Observation of the sling effect. *New J. Phys.* **15**, 083051.
- BOIVIN, M., SIMONIN, O. & SQUIRES, K. D. 1998 Direct numerical simulation of turbulence modulation by particles in isotropic turbulence. *J. Fluid Mech.* **375**, 235–263.
- BORDÁS, R., ROLOFF, CH., THÉVENIN, D. & SHAW, R. A. 2013 Experimental determination of droplet collision rates in turbulence. *New J. Phys.* **15** (4), 045010.
- BOSSE, T. & KLEISER, L. 2006 Small particles in homogeneous turbulence: settling velocity enhancement by two-way coupling. *Phys. Fluids* **18**, 027102.
- BRAGG, A. B. & COLLINS, L. R. 2014 New insights from comparing statistical theories for inertial particles in turbulence: I. Spatial distribution of particles. *New J. Phys.* **16**, 055013.
- BRAGG, A. D., IRELAND, P. J. & COLLINS, L. R. 2015 Mechanisms for the clustering of inertial particles in the inertial range of isotropic turbulence. *Phys. Rev. E* **92** (2), 023029.
- CALZAVARINI, E., KERSCHER, M., LOHSE, D. & TOSCHI, F. 2008 Dimensionality and morphology of particle and bubble clusters in turbulent flow. *J. Fluid Mech.* **607**, 13–24.
- CARTER, D. W. & COLETTI, F. 2017 Scale-to-scale anisotropy in homogeneous turbulence. *J. Fluid Mech.* **827**, 250–284.
- CARTER, D. & COLETTI, F. 2018 Small-scale structure and energy transfer in homogeneous turbulence. *J. Fluid Mech.* **854**, 505–543.
- CARTER, D., PETERSEN, A., AMILI, O. & COLETTI, F. 2016 Generating and controlling homogeneous air turbulence using random jet arrays. *Exp. Fluids* **57** (12), 189.
- CENCINI, M., BEC, J., BIFERALE, L., CELANI, A., LANOTTE, A. S., MUSACCHIO, S. & TOSCHI, F. 2006 Dynamics and statistics of heavy particles in turbulent flows. *J. Turbul.* **7**, N36.
- CHEN, L., GOTO, S. & VASSILICOS, J. C. 2006 Turbulent clustering of stagnation points and inertial particles. *J. Fluid Mech.* **553**, 143–154.
- CHUN, J., KOCH, D. L., RANI, S. L., AHLUWALIA, A. & COLLINS, L. R. 2005 Clustering of aerosol particles in isotropic turbulence. *J. Fluid Mech.* **536**, 219–251.
- CISSE, M., HOMANN, H. & BEC, J. 2013 Slipping motion of large neutrally buoyant particles in turbulence. *J. Fluid Mech.* **735**, R1.
- CLIFT, R., GRACE, J. & WEBER, M. E. 2005 *Bubbles, Drops and Particles*. Dover.
- COLEMAN, S. W. & VASSILICOS, J. C. 2009 A unified sweep-stick mechanism to explain particle clustering in two- and three-dimensional homogeneous, isotropic turbulence. *Phys. Fluids* **21**, 113301.
- COLETTI, F., TOLoui, M., FONG, K. O., NEMES, A. & BAKER, L. 2016 Volumetric distribution and velocity of inertial particles in a turbulent channel flow. In *18th International Symposium on Application of Laser and Imaging Techniques to Fluid Mechanics, Lisbon, Portugal*.
- CSANADY, G. T. 1963 Turbulent diffusion of heavy particles in the atmosphere. *J. Atmos. Sci.* **20** (3), 201–208.
- DÁVILA, J. & HUNT, J. C. R. 2001 Settling of small particles near vortices and in turbulence. *J. Fluid Mech.* **440**, 117–145.
- DEJOAN, A. & MONCHAUX, R. 2013 Preferential concentration and settling of heavy particles in homogeneous turbulence. *Phys. Fluids* **25** (1), 013301.
- EATON, J. K. 2009 Two-way coupled turbulence simulations of gas-particle flows using point-particle tracking. *Intl J. Multiphase Flow* **35** (9), 792–800.

- EATON, J. K. & FESSLER, J. R. 1994 Preferential concentration of particles by turbulence. *Intl J. Multiphase Flow* **20** (1), 169–209.
- ELGHOBASHI, S. 1994 On predicting particle-laden turbulent flows. *Appl. Sci. Res.* **52** (4), 309–329.
- ELGHOBASHI, S. & TRUESDELL, G. C. 1992 Direct simulation of particle dispersion in decaying isotropic turbulence. *J. Fluid Mech.* **242**, 655–700.
- ELGHOBASHI, S. & TRUESDELL, G. C. 1993 On the two way interaction between homogeneous turbulence and dispersed solid particles. I. Turbulence modification. *Phys. Fluids A* **5** (7), 1790–1801.
- ESMAILY-MOGHADAM, M. & MANI, A. 2016 Analysis of the clustering of inertial particles in turbulent flows. *Phys. Rev. Fluids* **1**, 084202.
- FALCONER, K. 2003 *Fractal Geometry Mathematical Foundations and Applications*. Wiley.
- FALKOVICH, G., FOUXON, A. & STEPANOV, M. G. 2002 Acceleration of rain initiation by cloud turbulence. *Nature* **419**, 151–154.
- FERENC, J.-S. & NÉDA, Z. 2007 On the size distribution of Poisson Voronoï cells. *Physica A* **385** (2), 518–526.
- FERRANTE, A. & ELGHOBASHI, S. 2003 On the physical mechanisms of two-way coupling in particle-laden isotropic turbulence. *Phys. Fluids* **15** (2), 315–329.
- FESSLER, J. R., KULICK, J. D. & EATON, J. K. 1994 Preferential concentration of heavy particles in a turbulent channel flow. *Phys. Fluids* **6**, 3742.
- FISCALETTI, D., WESTERWEEL, J. & ELSINGA, G. E. 2014 Long-range  $\mu$ PIV to resolve the small scales in a jet at high Reynolds number. *Exp. Fluids* **55**, 1812.
- FORNARI, W., PICANO, F. & BRANDT, L. 2016 Sedimentation of finite-size spheres in quiescent and turbulent environments. *J. Fluid Mech.* **788**, 640–669.
- FRANKEL, A., POURANSARI, H., COLETTI, F. & MANI, A. 2016 Settling of heated particles in homogeneous turbulence. *J. Fluid Mech.* **792**, 869–893.
- GAO, H., LI, H. & WANG, L.-P. 2013 Lattice Boltzmann simulation of turbulent flow laden with finite-size particles. *Comput. Maths Applics.* **65** (2), 194–210.
- GARRETT, T. J. & YUTER, S. E. 2014 Observed influence of riming, temperature, and turbulence on the fallspeed of solid precipitation. *Geophys. Res. Lett.* **41** (18), 6515–6522.
- GERASHCHENKO, S., SHARP, N. S., NEUSCAMMAN, S. & WARHAFT, Z. 2008 Lagrangian measurements of inertial particle accelerations in a turbulent boundary layer. *J. Fluid Mech.* **617**, 225–281.
- GIBERT, M., XU, H. & BODENSCHATZ, E. 2012 Where do small, weakly inertial particles go in a turbulent flow. *J. Fluid Mech.* **698**, 160–167.
- GOOD, G. H., GERASHCHENKO, S. & WARHAFT, Z. 2012 Intermittency and inertial particle entrainment at a turbulent interface: the effect of the large-scale eddies. *J. Fluid Mech.* **694**, 371–398.
- GOOD, G. H., IRELAND, P. J., BEWLEY, G. P. & BODENSCHATZ, E. 2014 Settling regimes of inertial particles in isotropic turbulence. *J. Fluid Mech.* **759**, R3.
- GORE, R. A. & CROWE, C. T. 1991 Modulation of turbulence by a dispersed phase. *Trans. ASME J. Fluids Engng* **113** (2), 304–307.
- GOTO, S. & VASSILICOS, J. C. 2006 Self-similar clustering of inertial particles and zero-acceleration points in fully developed two-dimensional turbulence. *Phys. Fluids* **18**, 115103.
- GOTO, S. & VASSILICOS, J. C. 2008 Sweep-stick mechanism of heavy particle clustering in fluid turbulence. *Phys. Rev. Lett.* **100**, 054503.
- DE GRAFF, D. B. & EATON, J. K. 2000 Reynolds-number scaling of the flat-plate turbulent boundary layer. *J. Fluid Mech.* **422**, 319–346.
- GUALA, M., LIBERZON, A., HOYER, K., TSINOBER, A. & KINZELBACH, W. 2008 Experimental study on clustering of large particles in homogeneous turbulent flow. *J. Turbul.* **9**, N34.
- GUALTIERI, P., SARDINA, G., PICANO, F. & CACCIOLA, C. M. 2013 Clustering and turbulence modulation in particle-laden shear flows. *J. Fluid Mech.* **715**, 134–162.
- GUALTIERI, P., SARDINA, G., PICANO, F. & CACCIOLA, C. M. 2015 Exact regularized point particle method for multiphase flows in the two-way coupling regime. *J. Fluid Mech.* **773**, 520–561.

- GUSTAVSSON, K. & MEHLIG, B. 2016 Statistical models for spatial patterns of heavy particles in turbulence. *Adv. Phys.* **65** (1), 1–57.
- GUSTAVSSON, K., VAJEDI, S. & MEHLIG, B. 2014 Clustering of particles falling in a turbulent flow. *Phys. Rev. Lett.* **112**, 214501.
- HASSAN, Y. A., BLANCHAT, T. K. JR. & SEELEY, C. H. 1992 PIV flow visualisation using particle tracking techniques. *Meas. Sci. Technol.* **3** (7), 633.
- HEARST, R. J., BUXTON, O. R. H., GANAPATHISUBRAMANI, B. & LAVOIE, P. 2012 Experimental estimation of fluctuating velocity and scalar gradients in turbulence. *Exp. Fluids* **53** (4), 925–942.
- HETSRONI, G. 1989 Particles–turbulence interaction. *Intl J. Multiphase Flow* **15** (5), 735–746.
- HOLTZER, G. L. & COLLINS, L. R. 2002 Relationship between the intrinsic radial distribution function for an isotropic field of particles and lower-dimensional measurements. *J. Fluid Mech.* **459**, 93–102.
- HORWITZ, J. A. K. & MANI, A. 2016 Accurate calculation of Stokes drag for point particle tracking in two-way coupled flows. *J. Comput. Phys.* **318** (1), 85–109.
- HUCK, P. D., BATESON, C., VOLK, R., CARTELLIER, A., BOURGOIN, M. & ALISEDA, A. 2018 The role of collective effects on settling velocity enhancement for inertial particles in turbulence. *J. Fluid Mech.* **846**, 1059–1075.
- HUNT, J. C. R., WRAY, A. A. & MOIN, P. 1988 Eddies, streams, and convergence zones in turbulent flows. In *Studying Turbulence Using Numerical Simulation Databases*, 2. *Proceedings of the 1988 Summer Program*.
- HWANG, W. & EATON, J. K. 2006a Homogeneous and isotropic turbulence modulation by small heavy ( $st \sim 50$ ) particles. *J. Fluid Mech.* **564**, 361–393.
- HWANG, W. & EATON, J. K. 2006b Turbulence attenuation by small particles in the absence of gravity. *Intl J. Multiphase Flow* **32** (12), 1386–1396.
- IRELAND, P. J., BRAGG, A. D. & COLLINS, L. R. 2016a The effect of Reynolds number on inertial particle dynamics in isotropic turbulence. Part 1. Simulations without gravitational effects. *J. Fluid Mech.* **796**, 617–658.
- IRELAND, P. J., BRAGG, A. D. & COLLINS, L. R. 2016b The effect of Reynolds number on inertial particle dynamics in isotropic turbulence. Part 2. Simulations with gravitational effects. *J. Fluid Mech.* **796**, 617–658.
- IRELAND, P. J. & DESJARDINS, O. 2017 Improving particle drag predictions in Euler–Lagrange simulations with two-way coupling. *J. Comput. Phys.* **338** (1), 405–430.
- ISHIMA, T., HISHDIA, K. & MAEDA, M. 1993 Effect of particle residence time on particle dispersion in a plane mixing layer. *J. Fluids Engng* **115** (4), 751–759.
- JENNY, P., ROEKAERTS, D. & BEISHUIZEN, N. 2012 Modeling of turbulent dilute spray combustion. *Prog. Energy Combust. Sci.* **38** (6), 846–887.
- DE JONG, J., SALAZAR, J. P. L. C., WOODWARD, S. H., COLLINS, L. R. & MENG, H. 2010 Measurement of inertial particle clustering and relative velocity statistics in isotropic turbulence using holographic imaging. *Intl J. Multiphase Flow* **36** (4), 324–332.
- KAWANISI, K. & SHIOZAKI, R. 2008 Turbulent effects on the settling velocity of suspended sediment. *J. Hydraul. Engng ASCE* **134** (2), 261–266.
- KHALITOV, D. A. & LONGMIRE, E. K. 2002 Simultaneous two-phase PIV by two-parameter phase discrimination. *Exp. Fluids* **32** (2), 252–268.
- KHALITOV, D. A. & LONGMIRE, E. K. 2003 Effect of particle size on velocity correlations in turbulent channel flow. In *ASME/JSME 2003 4th Joint Fluids Summer Engineering Conference*, vol. 1: Fora, parts A, B, C, and D.
- KIDANEMARIAM, A. G., CHAN-BRAUN, C., DOYCDEV, T. & UHLMANN, M. 2013 Direct numerical simulation of horizontal open channel flow with finite-size, heavy particles at low solid volume fraction. *New J. Phys.* **15**, 025031.
- KIGER, K. T. & PAN, C. 2000 PIV technique for the simultaneous measurement of dilute two-phase flows. *Trans. ASME J. Fluids Engng* **122** (4), 811–818.
- KIGER, K. T. & PAN, C. 2002 Suspension and turbulence modification effects of solid particulates on a horizontal turbulent channel flow. *J. Turbul.* **3**, 19.

- KULICK, J. D., FESSLER, J. R. & EATON, J. K. 1994 Particle response and turbulence modification in fully developed channel flow. *J. Fluid Mech.* **277**, 109–134.
- LÁZARO, B. J. & LASHERAS, J. C. 1989 Particle dispersion in a turbulent, plane, free shear layer. *Phys. Fluids A* **1**, 1035–1044.
- LONGMIRE, E. K. & EATON, J. K. 1992 Structure of a particle-laden round jet. *J. Fluid Mech.* **236**, 217–257.
- LOZANO-DURÁN, A., FLORES, O. & JIMÉNEZ, J. 2012 The three-dimensional structure of momentum transfer in turbulent channels. *J. Fluid Mech.* **694**, 100–130.
- LUCCI, F., FRRANTE, A. & ELGHOBASHI, S. 2010 Modulation of isotropic turbulence by particles of Taylor length-scale size. *J. Fluid Mech.* **650**, 5–55.
- MARUSIC, I. & KUNKEL, G. J. 2003 Streamwise turbulence intensity formulation for flat-plate boundary layers. *Phys. Fluids* **15**, 2461.
- MATSUDE, K., ONISHI, R. & TAKAHASHI, K. 2017 Influence of gravitational settling on turbulent droplet clustering and radar reflectivity factor. *Flow Turbul. Combust.* **98** (1), 327–340.
- MAXEY, M. R. 1987 The gravitational settling of aerosol particles in homogeneous turbulence and random flow fields. *J. Fluid Mech.* **174**, 441–465.
- MAXEY, M. R. & CORRSIN, S. 1986 Free access gravitational settling of aerosol particles in randomly oriented cellular flow fields. *J. Atmos. Sci.* **43**, 1112–1134.
- MAXEY, M. R. & RILEY, J. J. 1983 Equation of motion for a small rigid sphere in a nonuniform flow. *Phys. Fluids* **26** (4), 883–889.
- MEI, R. 1994 Effect of turbulence on the particle settling velocity in the nonlinear drag range. *Int'l J. Multiphase Flow* **20** (2), 273–284.
- MEI, R., ADRIAN, R. J. & HANRATTY, T. J. 1991 Particle dispersion in isotropic turbulence under Stokes drag and Basset force with gravitational settling. *J. Fluid Mech.* **225**, 481–495.
- MOISY, F. & JIMÉNEZ, J. 2004 Geometry and clustering of intense structures in isotropic turbulence. *J. Fluid Mech.* **513**, 111–133.
- MONCHAUX, R., BOURGOIN, M. & CARTELLIER, A. 2010 Preferential concentration of heavy particles: a Voronoï analysis. *Phys. Fluids* **22** (10), 103304.
- MONCHAUX, R., BOURGOIN, M. & CARTELLIER, A. 2012 Analyzing preferential concentration and clustering of inertial particles in turbulence. *Int'l J. Multiphase Flow* **40**, 1–18.
- MONCHAUX, R. & DEJOAN, A. 2017 Settling velocity and preferential concentration of heavy particles under two-way coupling effects in homogeneous turbulence. *Phys. Rev. Fluids* **2**, 104302.
- NASO, A. & PROSPERETTI, A. 2010 The interaction between a solid particle and a turbulent flow. *New J. Phys.* **12** (3), 033040.
- NEMES, A., COLETTI, F., FONG, K. O. & TOLOUI, M. 2016 Experimental observation of three-dimensional particle clustering in turbulent channel flow. In *International Conference on Multiphase Flows, Florence, Italy*.
- NEMES, A., DASARI, T., HONG, J., GUALA, M. & COLETTI, F. 2017 Snowflakes in the atmospheric surface layer: observation of particle turbulence dynamics. *J. Fluid Mech.* **814**, 592–613.
- NEMES, A., JACONO, D. L., BLACKBURN, H. M. & SHERIDAN, J. 2015 Mutual inductance of two helical vortices. *J. Fluid Mech.* **774**, 298–310.
- NIELSEN, P. 1993 Turbulence effects on the settling of suspended particles. *J. Sedim. Res.* **63** (5), 835–838.
- OBLIGADO, M., TEITELBAUM, T., CARTELLIER, A., MININNI, P. & BOURGOIN, M. 2014 Preferential concentration of heavy particles in turbulence. *J. Turbul.* **15** (5), 293–310.
- OHMI, K. & LI, H. Y. 2000 Particle-tracking velocimetry with new algorithms. *Meas. Sci. Technol.* **11** (6), 603.
- PAOLA, G. D., KIM, I. S. & MASTORAKOS, E. 2009 Second-order conditional moment closure simulations of autoignition of an n-heptane plume in a turbulent coflow of heated air. *Flow Turbul. Combust.* **82** (4), 455.
- PARIS, A. D. 2001 Turbulence attenuation in a particle-laden channel flow. PhD thesis, Stanford University.
- PERRY, A. E. & CHONG, M. S. 1994 Topology of flow patterns in vortex motions and turbulence. *Appl. Sci. Res.* **53** (3–4), 357–374.

- POELMA, C. & OOMS, G. 2006 Particle–turbulence interaction in a homogeneous, isotropic turbulent suspension. *ASME Appl. Mech. Rev.* **59** (2), 78–90.
- POELMA, C., WESTERWEEL, J. & OOMS, G. 2007 Particle–fluid interactions in grid-generated turbulence. *J. Fluid Mech.* **589**, 315–351.
- RABENCOV, B. & VAN HOUT, R. 2015 Voronoï analysis of beads suspended in a turbulent square channel flow. *Intl J. Multiphase Flow* **68**, 10–13.
- READE, W. C. & COLLINS, L. R. 2000 Effect of preferential concentration on turbulent collision rates. *Phys. Fluids* **12**, 2530.
- REEKS, M. W. 1977 On the dispersion of small particles suspended in an isotropic turbulent fluid. *J. Fluid Mech.* **83** (3), 529–546.
- ROGERS, C. B. & EATON, J. K. 1991 The effect of small particles on fluid turbulence in a flat plate, turbulent boundary layer in air. *Phys. Fluids A* **3** (5), 928–937.
- ROSA, B., PARISHANI, H., AYALA, O. & WANG, L.-P. 2016 Settling velocity of small inertial particles in homogeneous isotropic turbulence from high-resolution DNS. *Intl J. Multiphase Flow* **83**, 217–231.
- RUDOFF, R. & BACHALO, W. 1988 Direct particle fluid simulation of Kolmogorov-length-scale size particles in decaying isotropic turbulence measurements of droplet drag coefficients in a polydispersed turbulent flow field. In *26th Aerospace Sciences Meeting. Reno, NV, USA*.
- SABBAN, L. & VAN HOUT, R. 2011 Measurements of pollen grain dispersal in still air and stationary, near homogeneous, isotropic turbulence. *J. Aero. Sci.* **42** (12), 867–882.
- SAHU, S., HARDALUPAS, Y. & TAYLOR, A. M. K. P. 2014 Droplet turbulence interaction in a confined polydispersed spray: effect of droplet size and flow length scales on spatial droplet gas velocity correlations. *J. Fluid Mech.* **741**, 98–138.
- SAHU, S., HARDALUPAS, Y. & TAYLOR, A. M. K. P. 2016 Droplet turbulence interaction in a confined polydispersed spray: effect of turbulence on droplet dispersion. *J. Fluid Mech.* **794**, 267–309.
- SALAZAR, J. P. L. C. & COLLINS, L. R. 2012 Inertial particle acceleration statistics in turbulence: effects of filtering, biased sampling, and flow topology. *Phys. Fluids* **24**, 083302.
- SALAZAR, J. P. L. C., DE JONG, J., CAO, L. & WOODWARD, S. H. 2008 Experimental and numerical investigation of inertial particle clustering in isotropic turbulence. *J. Fluid Mech.* **600**, 245–256.
- SAW, E.-W., BEWLEY, G. P., BODENSCHATZ, E., RAY, S. S. & BEC, J. 2014 Extreme fluctuations of the relative velocities between droplets in turbulent airflow. *Phys. Fluids* **26** (11), 111702.
- SAW, E.-W., DEBUE, P., KUZZAY, D., DAVIAUD, F. & DUBRULLE, B. 2018 On the universality of anomalous scaling exponents of structure functions in turbulent flows. *J. Fluid Mech.* **837**, 657–669.
- SAW, E. W., SHAW, R. A., AYYALASOMAYAJULA, S., CHUANG, P. Y. & GYLASON, A. 2008 Inertial clustering of particles in high-Reynolds-number turbulence. *Phys. Rev. Lett.* **100** (21), 214501.
- SAW, E.-W., SHAW, R. A., SALAZAR, J. P. L. C. & COLLINS, L. R. 2012 Spatial clustering of polydisperse inertial particles in turbulence: II. Comparing simulation with experiment. *New J. Phys.* **14** (10), 105031.
- SCHANZ, D., GESEMANN, S. & SCHRÖDER, A. 2016 Shake-the-box: Lagrangian particle tracking at high particle image densities. *Exp. Fluids* **57** (5), 70.
- SCHNEIDERS, L., MEINKE, M. & SCHRODER, W. 2017 Direct particle-fluid simulation of Kolmogorov-length-scale size particles in decaying isotropic turbulence. *J. Fluid Mech.* **819**, 188–227.
- SHAW, R. A. 2003 Particle–turbulence interactions in atmospheric clouds. *Annu. Rev. Fluid Mech.* **35**, 183–227.
- SOLDATI, A. & MARCHIOLI, C. 2009 Physics and modelling of turbulent particle deposition and entrainment: review of a systematic study. *Intl J. Multiphase Flow* **35** (9), 827–839.
- SQUIRES, K. D. & EATON, J. K. 1990 Particle response and turbulence modification in isotropic turbulence. *Phys. Fluid A* **2**, 1191–1203.
- SQUIRES, K. D. & EATON, J. K. 1991a Measurements of particles dispersion obtained from direct numerical simulations of isotropic turbulence. *J. Fluid Mech.* **226**, 1–35.

- SQUIRES, K. D. & EATON, J. K. 1991b Preferential concentration of particles by turbulence. *Phys. Fluids A* **3** (5), 1169–1178.
- SUMBEKOVA, S., CARTELLIER, A., ALISEDA, A. & BOURGOIN, M. 2017 Preferential concentration of inertial sub-Kolmogorov particles: the roles of mass loading of particles, Stokes numbers, and Reynolds numbers. *Phys. Rev. Fluids* **2**, 024302.
- SUNDARAM, S. & COLLINS, L. R. 1997 Collision statistics in an isotropic particle-laden turbulent suspension. Part 1. Direct numerical simulations. *J. Fluid Mech.* **335**, 75–109.
- SUNDARAM, S. & COLLINS, L. R. 1999 A numerical study of the modulation of isotropic turbulence by suspended particles. *J. Fluid Mech.* **379**, 105–143.
- TAGAWA, Y., MERCADO, J. M., PRAKASH, V. N., CALZAVARINI, E., SUN, C. & LOHSE, D. 2012 Three-dimensional Lagrangian Voronoï analysis for clustering of particles and bubbles in turbulence. *J. Fluid Mech.* **693**, 201–215.
- TANAKA, T. & EATON, J. K. 2008 Classification of turbulence modification by dispersed spheres using a novel dimensionless number. *Phys. Rev. Lett.* **101**, 114502.
- TANAKA, T. & EATON, J. K. 2010 Sub-Kolmogorov resolution particle image velocimetry measurements of particle-laden forced turbulence. *J. Fluid Mech.* **643**, 177–206.
- TANG, D. & MARANGONI, A. G. 2006 3D fractal dimension of fat crystal networks. *Chem. Phys. Lett.* **433** (1–3), 248–252.
- TENNETI, S. & SUBRAMANIAM, S. 2014 Particle-resolved direct numerical simulation for gas–solid flow model development. *Annu. Rev. Fluid Mech.* **46**, 199–230.
- TOOBY, P. F., WICK, G. L. & ISAACS, J. D. 1977 The motion of a small sphere in a rotating velocity field: a possible mechanism for suspending particles in turbulence. *J. Geophys. Res.* **82** (15), 2096–2100.
- UHLMANN, M. & DOYCDEV, T. 2014 Sedimentation of a dilute suspension of rigid spheres at intermediate Galileo numbers: the effect of clustering upon the particle motion. *J. Fluid Mech.* **752**, 310–348.
- VARIANO, E. A. & COWEN, E. A. 2008 A random-jet-stirred turbulence tank. *J. Fluid Mech.* **604**, 1–32.
- VOLK, R., CALZAVARINI, E., VERHILLE, G., LOHSE, D., MORDANT, N., PINTON, J.-F. & TOSCHI, F. 2008 Acceleration of heavy and light particles in turbulence: comparison between experiments and direct numerical simulations. *Physica D* **237** (14–17), 2084–2089.
- WANG, L.-P., AYALA, O. & GRABOWSKI, W. W. 2007 Effects of aerodynamic interactions on the motion of heavy particles in a bidisperse suspension. *J. Turbul.* **8**, N25.
- WANG, L.-P. & MAXEY, M. R. 1993 Settling velocity and concentration distribution of heavy particles in homogeneous isotropic turbulence. *J. Fluid Mech.* **256**, 27–68.
- WANG, L.-P. & STOCK, D. E. 1993 Dispersion of heavy particles by turbulent motion. *J. Atmos. Sci.* **50**, 1897–1913.
- WANG, L.-P., WEXLER, A. S. & ZHOU, Y. 2000 Statistical mechanical description and modelling of turbulent collision of inertial particles. *J. Fluid Mech.* **415**, 117–153.
- WARNICA, W. D., RENKSIZBULUT, M. & STRONG, A. B. 1995 Drag coefficients of spherical liquid droplets. Part 2. Turbulent gaseous fields. *Exp. Fluids* **18** (4), 265–276.
- WELLS, M. R. & STOCK, D. E. 1983 The effects of crossing trajectories on the dispersion of particles in a turbulent flow. *J. Fluid Mech.* **136**, 31–62.
- WESTERWEEL, J. & SCARANO, F. 2005 Universal outlier detection for PIV data. *Exp. Fluids* **39**, 1096–1100.
- WILKINSON, M. & MEHLIG, B. 2005 Caustics in turbulent aerosols. *Europhys. Lett.* **71** (2), 186.
- WOITIEZ, E. J. P., JONKER, H. J. J. & PORTELA, L. 2009 On the combined effects of turbulence and gravity on droplet collisions in clouds: a numerical study. *J. Atmos. Sci.* **66** (7), 1926–1943.
- WOOD, A. M., HWANG, W. & EATON, J. K. 2005 Preferential concentration of particles in homogeneous and isotropic turbulence. *Int. J. Multiphase Flow* **31** (10–11), 1220–1230.
- WORTH, N. A., NICKELS, T. B. & SWAMINATHAN, N. 2010 A tomographic PIV resolution study based on homogeneous isotropic turbulence DNS data. *Exp. Fluids* **49** (3), 637–656.
- WU, J.-S. & FAETH, G. M. 1994 Sphere wakes at moderate Reynolds numbers in a turbulent environment. *AIAA J.* **32** (3), 535–54166.

- YANG, C. Y. & LEI, U. 1998 The role of the turbulent scales in the settling velocity of heavy particles in homogeneous isotropic turbulence. *J. Fluid Mech.* **371**, 179–205.
- YANG, T. S. & SHY, S. S. 2003 The settling velocity of heavy particles in an aqueous near-isotropic turbulence. *Phys. Fluids* **15** (4), 868–880.
- YANG, T. S. & SHY, S. S. 2005 Two-way interaction between solid particles and homogeneous air turbulence: particle settling rate and turbulence modification measurements. *J. Fluid Mech.* **526**, 171–216.
- YOSHIMOTO, H. & GOTO, S. 2007 Self-similar clustering of inertial particles in homogeneous turbulence. *J. Fluid Mech.* **577**, 275–286.
- YUDINE, M. I. 1959 Physical considerations on heavy-particle diffusion. *Adv. Geophys.* **6**, 185–191.
- ZAICHIK, L. I. & ALIPCHENKOV, V. M. 2009 Statistical models for predicting pair dispersion and particle clustering in isotropic turbulence and their applications. *New J. Phys.* **11**, 103018.
- ZAMANSKY, R., COLETTI, F., MASSOT, M. & MANI, A. 2016 Turbulent thermal convection driven by heated inertial particles. *J. Fluid Mech.* **809**, 390–437.
- ZHAO, L. H., MARCHIOLI, C. & ANDERSSON, H. I. 2012 Stokes number effects on particle slip velocity in wall-bounded turbulence and implications for dispersion models. *Phys. Fluids* **24**, 021705.